1

PM-1 3½"x4" PHOTOGRAPHIC MICROCOPY TARGET
NBS 1010a ANSI/ISO #2 EQUIVALENT
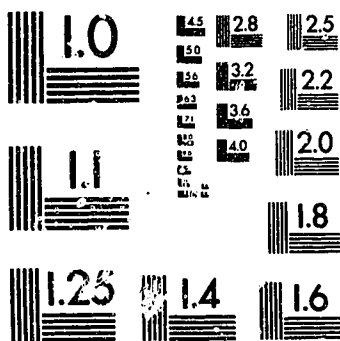
1.0

1.1

1.25

.45
.50
.56
.63
.71
.80
.89

2.8
3.2
3.6
4.0

1.4

2.5

2.2

2.0

1.8

1.6

NOTICE

AVIS

The quality of this microform is heavily dependent upon the quality of the original thesis submitted for microfilming. Every effort has been made to ensure the highest quality of reproduction possible.

La qualité de cette microforme dépend grandement de la qualité de la thèse soumise au microfilmage. Nous avons tout fait pour assurer une qualité supérieure de reproduction.

If pages are missing, contact the university which granted the degree.

S'il manque des pages, veuillez communiquer avec l'université qui a conféré le grade.

Some pages may have indistinct print especially if the original pages were typed with a poor typewriter ribbon or if the university sent us an inferior photocopy.

La qualité d'impression de certaines pages peut laisser à désirer, surtout si les pages originales ont été dactylographiées à l'aide d'un ruban usé ou si l'université nous a fait parvenir une photocopie de qualité inférieure.

Canada

University of Alberta

Numerical and Experimental Analysis of Al_2O_3 Particulate Reinforced 6061

Aluminum Alloy Under Multiaxial and Nonproportional Cyclic Loads

by

© Garret Meijer

A thesis submitted to the Faculty of Graduate Studies and Research in partial

fulfillment of the requirements for the degree of Master of Science

Department of Mechanical Engineering

Edmonton, Alberta

Spring, 1995

ISBN 0-612-01638-2

Canada

University of Alberta

Library Release Form

Name of Author: Garret Meijer

Title of Thesis: Numerical and Experimental Analysis of Al_2O_3 Particulate Reinforced 6061 Aluminum Alloy Under Multiaxial and Nonproportional Cyclic Loads

Degree: Master of Science

Year this Degree Granted: 1995

Permission is hereby granted to the University of Alberta Library to reproduce single copies of this thesis and to lend or sell such copies for private, scholarly, of scientific research purposes only.

The author reserves all other publication and other rights in association with the copyright in the thesis, and except as hereinbefore provided, neither the thesis nor any substantial portion thereof may be printed or otherwise reproduced in any material form whatever without the author's prior written permission.
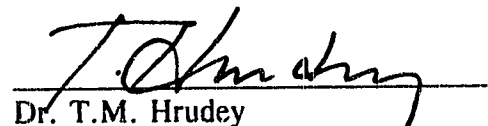
Garret Meijer
R.R. #1
Bon Accord, Alberta
T0A 0K0

April 21, 95

University of Alberta

Faculty of Graduate Studies and Research

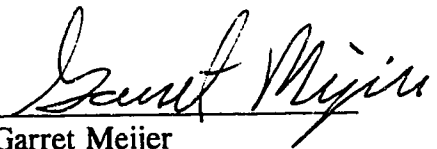The undersigned certify that they have read, and recommend to the Faculty of Graduate Studies and Research for acceptance, a thesis entitled **Numerical and Experimental Analysis of Al₂O₃ Particulate Reinforced 6061 Aluminum Alloy Under Multiaxial and Nonproportional Cyclic Loads** submitted by Garret Meijer in partial fulfillment of the requirements for the degree of Master of Science.

Dr. F. Ellyin

Dr. K.R. Fyfe

Dr. T.M. Hrudey

Dr. C. Li

95-04-20

Abstract

The behaviour of Al_2O_3 particulate reinforced 6061 aluminum alloy under multiaxial and nonproportional loads was studied using material tests and finite element analysis. Multiaxial loads were applied to thin walled tubular specimens by applying an axial load as well as a differential internal/external pressure. The numerical analysis of cyclic multiaxial behaviour was completed using the Ellyin and Xia constitutive relation to model the aluminum alloy. A comparison of the experimental and numerical results shows that the unit cell model with a spherical inclusion produces accurate results for uniaxial, equibiaxial and 90° out of phase biaxial cyclic loads. It was also shown that cube shaped inclusions produce greater initial hardening than spheres due to the high stress concentrations and localized plasticity. An analysis of thermal residual stresses, due to the difference in the coefficients of thermal expansion of the two materials, showed that the residual stresses can lead to nonlinear monotonic stress-strain behaviour of the composite but this effect dissipates rapidly after the first load reversal.

Acknowledgements

Table of Contents

List of Tables

List of Figures

1 Introduction

1.1 An Introduction to Metal Matrix Composites.

Metal matrix composites are a new class of engineered materials being considered for a wide variety of applications in the automotive and aerospace industries. These composites can be designed by controlling the material, geometry and amount of reinforcement added to the selected matrix. In this manner, the overall properties of the composite can be optimized for each application. The idea of metal matrix composites is not new but only recently have improved production methods allowed the production of a useful composite in large quantities. There is an increasing number of papers available describing the behaviour of metal matrix composites. Most recently there has been an abundance of research on discontinuous metal matrix composites. Most results, however, are limited to simple uniaxial loads. The results contained herein are part of an effort to determine the response of particulate reinforced metal matrix composites subjected to multiaxial monotonic and cyclic loads.

1.1.1 Materials Used to Produce Metal Matrix Composites.

There are numerous combinations of materials that can be used to produce a metal matrix composite. Table 1.1 illustrates the large number of materials and combinations which have been considered to produce new composites by a variety of methods including gravity casting, ingot casting, powder metallurgy, infiltration and diffusion bonding (Arsenault and Everett, 1991). The properties of each material, the matrix and reinforcement, must be considered when a metal matrix composite is produced.

1

Table 1.1: Successful Matches of reinforcement and matrix materials in metal matrix composites and fabrication methods used (Boardman, 1990).

	Reinforcement							
	Discontinuous			Continuous				
Matrix	Al_2O_3	SiC	W	Al_2O_3	B	C	SiC	WC
Al	C, PS	C, IC, PS	C	C, MI	C, DB	C, MI, DB	C, PS	C
Cu	C, PS	C, PS		C		DB	C	MI
Fe			C, PS					
Mg	C, PS	C, IC, PS		C	C	C, DB	C	
Ti	DB	DB			C		DB	DB

Fabrication Methods
Gravity Casting   C
Ingot Cast and Formed   IC
Powder Sintering   PS
Metal Infiltration   MI
Diffusion Bonding   DB

As suggested by the name, the matrix is always a metal such as aluminum, steel, copper or titanium. Generally the composites strongly reflect the behaviour of the matrix thus making its selection very important. Often the most suitable material, without reinforcement, is selected and then improved by the addition of a second phase. Important properties in the matrix may be yield and ultimate strength, stiffness, ductility, fracture toughness and corrosion resistance.

The reinforcement may be a metal, ceramic or any material added to improve the properties of the matrix. For example carbon fibres may be added because of their lubricating properties. Very important considerations for the selection of a reinforcement material is the chemical compatibility with the matrix and bond strength. If the two materials react to produce a weak interface debonding may result in cracks and voids around the reinforcement.

1.1.2 Inclusion Geometry and Volume Fraction.

The possible inclusion shapes are divided into three categories; fibres, whiskers and particles. These are shown in Figure 1.1. Fibres are continuous reinforcement which run from one end of the component to the other without interruption. This produces a material with very anisotropic properties which is designed such that the reinforcement carries a large portion of the load. Fibre reinforced composites are produced by manually aligning the fibres between layers of the matrix material and these are then diffusion bonded. This process makes them very expensive. When short fibres are used, they are called whiskers. Generally whisker reinforced composites are isotropic unless the

3

whiskers are aligned by rolling or extrusion. Another form of reinforcement is particles which may be spheres, pl; 'elets or angular particles. Particles with sharp corners produce higher stresses and localized plasticity within the matrix which results in higher yield stresses than composites reinforced with spheres. Particulate reinforcement results in a composite which is isotropic, and therefore can be treated as most conventional materials and is relatively inexpensive to make. Particle reinforcement results in smaller plastic strains within the matrix than do whisker inclusions, and therefore demonstrate less hardening and lower flow stress but greater elongation to failure (Llorca, Needleman and Suresh, 1991). From this point on, all discussion will be concerning metal matrix composites containing particulate reinforcement like the material tested.

The size of the added reinforcement is an important consideration on strengthening as well as fracture toughness and fatigue life. It has been found that the yield strength, ultimate strength and strain to failure all decrease as the size of the reinforcement is increased. In fact, the increase in size causes a change in the deformation mechanism from planar slip due to shearing of the particles to wavy slip from dislocation bypassing (Shang and Ritchie, 1989). Larger particles are also believed to result in reduced residual stresses due to fewer subgrain boundaries and less particle interaction. Fracture studies have found that effective threshold stress intensity range, $\Delta K_{eff,th}$, is much larger for small particles therefore composites containing smaller particles have greater toughness. In the case of low stress fatigue crack growth, larger particles produce roughness induced closure which slows crack growth and therefore, $\Delta K_{eff,th}$, is increased. For large fatigue loads when no closure occurs, $\Delta K_{eff,th}$ decreases

4

(Shang and Ritchie, 1989). Results suggest that an even distribution of fine particles will provide the best properties.

Another important parameter which can be controlled is the volume fraction of reinforcement added. Tests clearly show that the yield stress, ultimate stress and stiffness increase and strain to failure decreases as the ratio is increased. The greater strength may be attributed to more particle interaction resulting in greater hardening (McDanels, 1985). The volume fraction is the dominant factor in increasing the elastic modulus since a larger amount of the load will be carried by the reinforcement.

1.1.3   Duralcan 20% Al$_2$O$_3$p 6061

The alumina-aluminum composite is being introduced to the automobile industry and is being used in components such as brake rotors, drive shafts and suspension components. It has also found applications in the aerospace industry and is currently being used for bicycle frames. The composites high specific stiffness and wear resistance make it suitable for these applications.

The material tested in this investigation was provided by Alcan Ltd. which is now producing alumina particulate reinforced aluminum in large quantities. The composite is made by adding the alumina particles 5 to 80 microns in size to the molten aluminum and is cast in billets. The material was supplied in the form of extruded tubes in the T6 solution treatment. An example of the 20% Al$_2$O$_3$ 6061-T6 composite is shown in Figure 1.2. The matrix material is 6061 aluminum which has the constituents as shown in Table 1.2.

5

Table 1.2: Constituents of 6061 aluminum alloy.

Constituent	% Mass
Si	0.4 - 0.8
Cu	0.15 - 0.4
Fe	0.7 max
Mn	0.15 max
Mg	0.8 - 1.2
Cr	0.04 - 0.35
Zn	0.25 max
Ti	0.15 max
Others	0.05 max each 0.15 max total
Al	Balance

Figure 1.3 shows an etched sample of 6061-T6 and clearly displays the grain structure. This series of aluminum has good formability, weldability, machinability and corrosion resistance. The large percentages of silicon and magnesium form Mg_2Si making this alloy heat treatable. During annealing the material is recrystallized and undergoes no natural age hardening later. The yield strength of the annealed aluminum depends more strongly on the temperature than annealing time thus oven temperature must be carefully monitored. The T6 heat treatment of this alloy is commonly used in industrial applications because it has the greatest strength but lowest corrosion resistance. This material displays large amounts of precipitation hardening with the first stages of precipitation at room temperature, however, overaging results in decrease in strength and hardness when artificially aged at too high a temperature for too long.

1.2 Methods of Strengthening in Particulate Reinforced Metal Matrix Composites.

There are two general philosophies of what mechanisms produce the added strength within the particle reinforced composite: 1) the transfer of the load to the stiff elastic reinforcement and 2) changes in the microstructure of the matrix due to the presence of the reinforcement. It is likely that these two general mechanisms act simultaneously to provide the composite with a much higher strength than the matrix material alone. The experimental values, however, may not be as large as those predicted by load transfer and microstructural changes because of relaxation occurring at stress concentrations in the matrix near the particles or in regions of high particle density.

7

Failure mechanisms which may occur include the nucleation of voids within the matrix, debonding of the matrix from the reinforcement and shear failure of the matrix (Llorca, Needleman and Suresh, 1991). The following is a brief discussion of the two strengthening philosophies.

1.2.1   Load Transfer

This philosophy is based on the belief that a significant part of an external load is passed from the matrix to the reinforcement. Loads may be transferred via normal loading, shear loading of both. These are the basis of the slab model and shear lag models.

1.2.1.1   The Slab Model

Load transfer is very important in fibre reinforced composites where the fibres are sufficiently long to be considered continuous throughout the component. In the slab model, the composite is considered to consist of the matrix material and a proportional amount of reinforcement. There is no consideration for size or shape of the reinforcement. Basic assumptions for the stress and strain fields are applied to determine axial and transverse properties. For example, when the reinforcement is fibres and it is assumed that the matrix and fibre axial strain is equal (Voigt Model), the strain balance produces

$$E_{CA} = (1-f)E_M + fE_I \qquad (1.1)$$

where f is the volume fraction of reinforcement, E_M, E_I and E_{CA} are the elastic moduli

8

of the matrix, reinforcement and composite in the direction parallel to the fibres respectively. Equation 1.1 is commonly called the 'Rule of Mixtures' and is quite accurate for fibre reinforced composites. When one assumes the transverse stress is equivalent in the two phases (Reuss Model) the resulting equation is

$$E_{CT} = \left[\frac{f}{E_I} + \frac{(1-f)}{E_M} \right]^{-1} \tag{1.2}$$

where E_{CT} is the elastic modulus of the composite perpendicular to the fibres. These equations, however, can not be applied to particulate reinforced composites. For example, for the case of aluminum (E = 69 500 MPa) reinforced with 20%v alumina (E = 450 000 MPa) these equations result in values of 145 600 MPa and 83 700 MPa respectively. The elastic modulus of the 20% Al_2O_3p 6061 composite from experimental values is near 100 000 MPa. Clearly the more complex stress distribution within the matrix due to the discontinuous reinforcement must be considered.

1.2.1.2   The Shear Lag Method

The shear lag method is based on an analytical model of load transfer from the matrix to the reinforcement by shear only. The model assumes a radial shear stress distribution surrounds a cylindrical particle. The stress field is found by equating the shear on concentric rings while the far field strain within the matrix is assumed to be uniform. The derivation is based on a hexagonal distribution but is not very sensitive to geometry so this case is used in general (Clyne and Withers, 1993). The stresses and strains predicted within the particle or short fibre are greatest at the middle and decrease

to towards the ends (Nardone and Prewo, 1985).

The shear lag model completely neglects the tensile loads transferred at the ends of the particle. This may be the case for large composite strains, when voids have nucleated near the tips, but the initial yielding is also dependent on the geometry (Kamat, Hirth and Mehrabian, 1989). Corrections have been added to the shear lag model to compensate for the load transferred at the particle ends. For example, one simple method is to, in effect, increase the length of the particle to add extra shear force transfer to account for the tensile loads (Nardone and Prewo, 1986). While this simple model does not consider the actual stress field around the particle, it has produced reasonable results for the yield strength of the composite.

Two other models which are based on the transfer of load, are the Eshelby method (Eshelby, 1957) for solving the stress field for ellipsoidal inclusions in an elastic matrix and the finite element method. Both of these methods will be described in greater detail in the following chapter.

1.2.2   Changes Within the Matrix Microstructure

The second area of focus in the study of strengthening in discontinuously reinforced metal matrix composites, is changes in the matrix microstructure due to the presence of the particles. Strengthening has been attributed primarily to two features: increased dislocation density and smaller subgrain size. Consideration has also been given to dispersion hardening but this is believed to be more important in the aging of the composite. Other mechanisms, such as the change in crystal structure of the matrix, are

10

not considered significant in the increase of strength in the composite.

Dislocations can be created in particulate reinforced metal matrix composites by cold working (Shi, Arsenault, Krawitz and Smith, 1993; Lee and Subramanian, 1993) but a method of generation more specific to these composites, is by thermal treatment. For the composite considered in this study, aluminum has a thermal coefficient of expansion of approximately $24 \times 10^{-6}/^{\circ}C$ and this value is $8 \times 10^{-6}/^{\circ}C$ for the alumina reinforcement. This large difference in the thermal coefficients of expansion, commonly called ΔCTE, results in large residual stresses near the particles after a temperature drop. Such a temperature drop may occur during processing, when the reinforcement is mixed in the molten metal and then cooled, or as part of a subsequent heat treatment. These residual stresses are relaxed by the generation of dislocations within the matrix around the particle. The nature of this mechanism has been studied by microscopy and analytical techniques (Christman and Suresh, 1987).

Extensive analysis of the microstructure of metal matrix composites show that the difference in coefficients of expansion lead to a much higher dislocation density within the matrix. The density is highest near the particles (Arsenault, Wang and Feng, 1991) but the generation of dislocations may be sufficient to cover the entire matrix (Taya, Lulay and Lloyd, 1991). It has clearly been shown that the number of dislocations is greater in composites of higher volume fractions and decreases as the size of the reinforcement is increased (Arsenault, Wang and Feng, 1991). Transmission electron microscope studies also show that most of the plastic deformation within the composite occurs in regions with higher than average volume fraction of reinforcement and a high

dislocation density. Thus one finds the same trends for dislocation density and strength with variations in the amount and size of reinforcement. Arsenault, Wang and Feng (1991) made a comparison of composite and a specimen of cold rolled matrix material. While the cold worked aluminum alloy had a much lower dislocation density than the composite, it experienced a much larger increase in strength over the unworked matrix than the composite. Clearly the increase in dislocation density cannot be used to explain the increased strength in metal matrix composites and other mechanisms must be considered.

An analytical model based on dislocation punching (Arsenault, 1991) is commonly used to determine the increase in strength. This very simple model is based on the volume fraction of reinforcement, particle size and crystal structure of the matrix. Results indicate that the residual stresses within the matrix are tensile. For spherical particles, the residual stress is purely hydrostatic tension which should have no effect on dislocation generation and therefore the yield point should be the same for compressive and tensile loads. Experimental results from others (Jain, MacEwen and Wu, 1994) and the results of a finite element analysis, provided in Chapter five, show that the tensile yield stress is actually greater than that in compression.

The decrease in subgrain size resulting from the addition of the reinforcement is believed to contribute to the extra strength of the composite. Microscope specimens show that the grain and subgrain size near the particles is significantly decreased. Strengthening may occur since the grain and subgrain boundaries act to limit dislocation movement (Llorca, 1994). This mechanism is not fully understood and estimates of increase in

strength due to this effect are based on empirical formulas.

Dispersion hardening is another mechanism which may contribute to the strength of particulate reinforced composites. The added reinforcement may resist the plastic flow of the matrix producing an internal back stress (Mori and Tanaka, 1973). The particles enhance dislocation development by acting as barriers resulting in dislocation build up and tangles. Clyne and Withers (1993) however, suggest that this mechanism applies to closely packed particles and may not be a factor at all since most of the reinforcement lies on grain boundaries. While it is not widely believed that the particles lend directly to the increased strength of the composite, they may have a secondary effect on the matrix. The high dislocation density around the reinforcement may provide additional nucleation sites for precipitates which are significant in dispersion hardening. This is explained by the fa. that the composite material ages much more quickly than the aluminum matrix whe alone (Christman and Suresh, 1988).

While the effects of load transfer and changes in the matrix microstructure have often been studied independently, it is most likely that they act together to produce the added strength in the composite. However failure mechanisms should also be explored. Mechanisms of failure may be very common throughout the composite due to high stress concentrations and imperfect reinforcement. While a combination of the mechanisms described, load transfer and changes in the microstructure, may over estimate strength, if the failure processes which are also occurring in the material are accounted for, the results may approach experimental values.
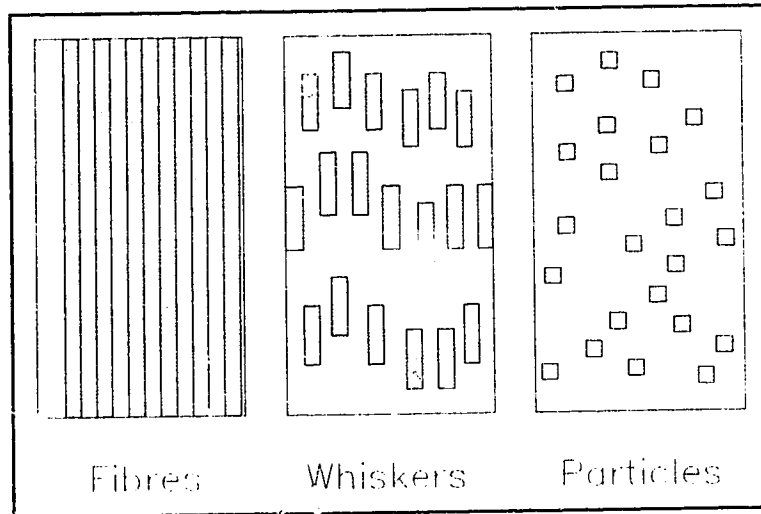
Figure 1.1: The three categories of inclusion shape.
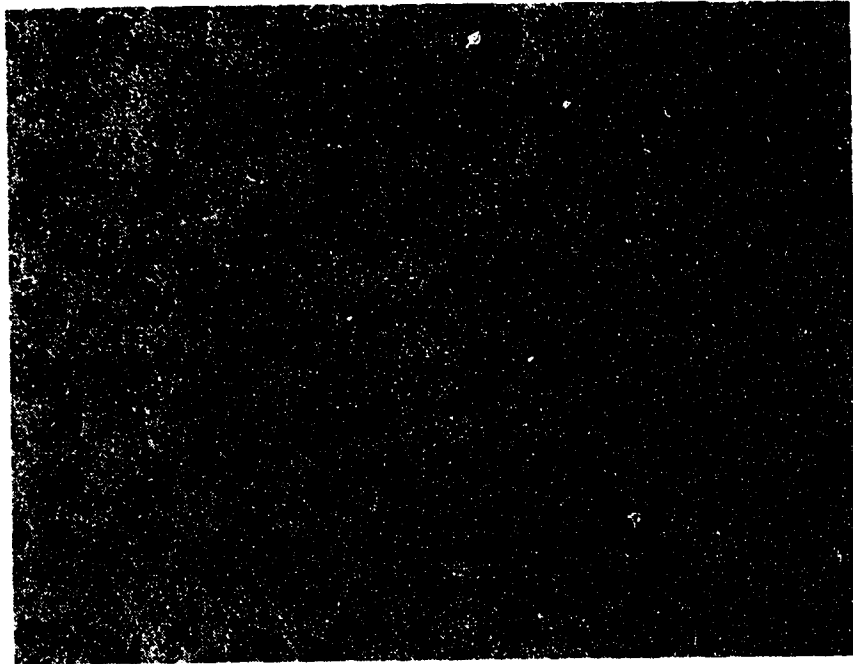
Figure 1.2: Micrograph of 20% Al₂O₃p 6061-T6 composite showing the reinforcement distribution.

Figure 1.3: Micrograph of 6061-T6 aluminum alloy etched to show the grain structure.

2 Methods of Modelling the Composite Materials

Numerous methods are used to estimate the behaviour of particulate reinforced metal matrix composites based on the material properties of the matrix and reinforcement on their own. These methods range from the simple rule of mixtures commonly used for fibre reinforced composites to complicated numerical methods such as finite element analysis. For particulate reinforced metal matrix composites, two methods of analysis are quite popular; the analytical Eshelby inclusion method and the numerical finite element method.

2.1 Eshelby's Solution

In the 1950's, J. D. Eshelby (1957) derived the equations for the stress field of a single elastic ellipsoidal inclusion in an elastic medium. This method is based on a cutting and welding procedure in which the particle is represented by one made of the matrix material which has the appropriate strain to have the same stress field as the original inclusion. The Eshelby solution is not limited to ellipsoidal inclusions, however in this case, the stress and strain distributions within the particle are uniform, thus an analytical solution is available. The original solution developed for a single inclusion in an infinite elastic matrix. The effects of the surrounding particles in a highly reinforced composite are added in Section 2.1.2.

2.1.1 The Eshelby Procedure

In this procedure, the inclusion is replaced by a suitably strained portion of matrix

16

material. This new inclusion will be termed a ghost inclusion. When this ghost inclusion is welded into the matrix no sliding occurs at the interface. The procedure is shown in Figure 2.1.

The inclusion region, with no deformations, is first cut from the elastically homogeneous matrix, A. It then undergoes a change in shape by $\epsilon = \epsilon^T$ as the constraint of the surrounding matrix is removed, B. Surface tractions are applied to the inclusion to return it to its original shape, C, and it is welded into the matrix, D, and the surface tractions are removed. This system then reaches equilibrium, E, at some constrained strain $\epsilon = \epsilon^C$.

The stress within the uniformly strained inclusion at point E is given by

$$\sigma_I = C_M(\epsilon^C - \epsilon^T) \qquad (2.1)$$

where C_M is the matrix stiffness tensor and ϵ^C and ϵ^T are related by

$$\epsilon^C = S\epsilon^T \qquad (2.2)$$

and the Eshelby tensor, S, is based on the aspect ratio of the ellipsoid and the value of Poisson's ratio. The Eshelby tensor for spherical particles is provided in Appendix A. Using Eq. 2.2, the stress in the inclusion (internal stress) is then found as a function of ϵ^T.

$$\sigma_I = C_M(S-I)\epsilon^T \qquad (2.3)$$

where I is the identity matrix. Thus, for this dilute system, the stress and strain within the inclusion can be calculated without considering the complicated stress distribution in the matrix.

Now an external load is applied. In an elastically homogeneous medium, the strain is the same throughout and the stress at each point is the sum of the applied stress and the internal stress. Thus for the ghost inclusion, which is made of the matrix material, the internal stress is

$$\sigma_I + \sigma^A = C_M(\epsilon^C - \epsilon^T) + C_M \epsilon^A \qquad (2.4)$$

This may also be expressed in terms of the properties of the true inclusion.

$$\sigma_I = C_I(\epsilon^C + \epsilon^A) \qquad (2.5)$$

At this point, the real and ghost inclusions can be interchanged without disturbing the matrix. It is then possible to find a stress free transformation strain ϵ^T, which is the same as in the real inclusion when the composite is under an applied load. The real inclusion and ghost inclusion can now be interchanged without disturbing the matrix. Using the Eshelby tensor and Equations 2.4 and 2.5, one can find the equivalent transformation strain associated with the misfit between the shapes of the inclusion and the hole which would occur if the two phases were subjected to the applied load independently.

$$\epsilon^T = -[(C_I - C_M)S + C_M]^{-1}(C_I - C_M)\epsilon^A \qquad (2.6)$$

This then yields

$$\sigma_I + \sigma^A = -C_M(S - I)[(C_I - C_M)S + C_M]^{-1}(C_I - C_M)\epsilon^A + C_M \epsilon^A \qquad (2.7)$$

The entire stress field around the particle is now defined.

2.1.2 Extension to a Non-Dilute system

While the solution given above describes the stress distribution around the particle, it is based upon one inclusion and the results are only applicable when the volume fraction is below 5% and the stresses are not influenced by the surrounding particles (Clyne and Withers, 1993). This solution will now be extended to include the influence of surrounding particles such as occurs in composites with greater amounts of reinforcement.

To maintain the balance of stresses, the composite distorts upon cutting, so as to provide an average matrix stress to oppose the inclusion stress. This is incorporated into the model by superposing a background stress which acts as if it were externally applied. The volume fraction is implemented as

$$(1-f)<\sigma>_M + f<\sigma>_i = 0 \tag{2.8}$$

and does not account for individual interactions, but is an average effect of the random distribution. For the case of an external load, the ghost inclusion is stressed by

$$\sigma_I + <\sigma>_M + \sigma^A = <\sigma>_I + \sigma^A \tag{2.9}$$

with the corresponding strain

$$\epsilon^C + \epsilon^A + <\epsilon>_M \tag{2.10}$$

The stress can then be expressed as

$$<\sigma>_I + \sigma^A = C_I(\epsilon^C + \epsilon^A + <\epsilon>_M) \tag{2.11}$$

or

$$<\sigma>_I + \sigma^A = C_M(\epsilon^C + \epsilon^A + <\epsilon>_M - \epsilon^T) \qquad (2.12)$$

These le·d to the term for the required transformation strain.

$$\epsilon^T = -\{(C_M - C_I)[S - f(S - I)] - C_M\}^{-1}(C_M - C_I)\epsilon^A \qquad (2.13)$$

From this, the mean stresses in the inclusion and matrix can be calculated using

$$<\sigma>_M = -fC_M(S - I)\epsilon^T \qquad (2.14)$$

and

$$<\sigma>_I = (1 - f)C_M(S - I)\epsilon^T \qquad (2.15)$$

The overall composite stiffness is related to the volume averaged composite strain under an applied load,

$$\sigma^A = C_C\overline{\epsilon_C^A} = C_C(\epsilon^A + <\epsilon>_C) \qquad (2.16)$$

In the matrix the local internal strains due to the inclusion average to zero therefore the overall strain consists of the mean matrix strain and the constrained strain within the inclusions.

$$<\epsilon>_C^A = <\epsilon>_M + f\epsilon^C \qquad (2.17)$$

The mean matrix strain found by considering the internal stress balance for the ghost composite, is:

$$(1 - f)C_M<\epsilon>_M + fC_M(<\epsilon>_M + \epsilon^C - \epsilon^T) = 0 \qquad (2.18)$$

which leads to

$$<\epsilon>_M = -f(\epsilon^C - \epsilon^T) = 0 \qquad (2.19)$$

so that

$$<\epsilon>_C^A = f\epsilon^T \qquad (2.20)$$

The overall composite strain is then given by

$$\overline{\epsilon_C^A} = \epsilon^A + f\epsilon^T \qquad (2.21)$$

Now substituting for ϵ^T we get

$$\overline{\epsilon_C^A} = \epsilon^A - f(C_M - C_I)[S - f(S - I)] - C_M)^{-1}(C_M - C_I)\epsilon^A \qquad (2.22)$$

The expression for the average stress then becomes

$$\sigma^A = C_C\left[C_M^{-1}\sigma^A - f(C_M - C_I)[S - f(S - I)] - C_M)^{-1}(C_M - C_I)C_M^{-1}\sigma^A\right] \qquad (2.23)$$

The composite stiffness tensor is then

$$C_C = \left[C_M^{-1} - f(C_I - C_M)[S - f(S - I)] - C_M)^{-1}(C_I - C_M)C_M^{-1}\right]^{-1} \qquad (2.24)$$

One can then find the axial modulus using $E_{3c} = 1/(C_{3c})^{-1}$.

Figure 2.2 shows the increase in stiffness of a composite made of Al_2O_3 (E = 450000 MPa, ν = 0.25) spheres and Aluminum (E = 69500 MPa, ν = 0.33) as the volume fraction of reinforcement is increased from 0 to 40%.

This is the basic elastic solution to Esheby's ellipsoidal inclusion problem. Numerous modifications to this solution have been made to add plasticity and other effects (Withers, Stobbs and Pedersen, 1989; Mochida, Taya and Lloyd, 1991; Arsenault and Taya, 1987; Corbin and Wilkinson, 1994).

21

2.2 The Finite Element Method

The use of finite element analysis to study composites has increased recently as computers have become more powerful and more complex software has become available. Finite element analysis is now used to study the effects of residual stresses as well as the response of particulate reinforced metal matrix composites under various complex loads. The only limit on the complexity of the model are the computer resources available. The effects of particle shape and aspect ratio and particle clustering have been studied (Christman, Needleman and Suresh, 1989). This is a significant advantage over analytical models which have only been solved for specific reinforcement geometries.

2.2.1 Application of the Periodic Array

Ideally one would like to analyze the composite component as one entity with one solution. For a discontinuous metal matrix composite it is not reasonable to do a detailed microstructural investigation since it contains a very large number of particles which vary in sizw from 5 to 80 microns arranged in a random manner. In order to do a detailed analysis, the problem must be greatly reduced.

The most significant simplifying assumption commonly adopted is that the composite is composed of a perfect array of identical unit cells. Each unit cell contains a particle of identical size and shape and a proportional amount of matrix material and will therefore, experience the same stresses and strains. In this investigation, each unit cell has size 2x2x2 and is 20% reinforcement by volume. These dimensions were chosen so theat the finite element model had sides of length 1. Therefore a spherical inclusion

22

will have a diameter of 1.451 and a cube inclusion will have sides of 1.170. Note that these dimensions are without units and the analysis is independent of the particle size.

This model assumes that the inclusions are perfectly aligned. From the simple array structure shown in Figure 2.3 one can then take a unit cell with the orientation which represents the appropriate load direction. The two sample unit cells shown; simple cubic and body centre cubic appear to be the limiting cases for estimateing the composite strength (see Kujawski, Xia and Ellyin, 1994). The simple cubic arrangement is used in this investigation and is the upper bound, the body centre cubic model is the lower bound. The true composite material will contain all the cases between and including these cases.

The selection of type of unit cell to be used in a finite element analysis is an important consideration. One can use a plane stress or plane strain two-dimensional model (Wang, Chen and Lloyd, 1993), an axisymmetric model (Tvergaard, 1990; Christman, Needleman and Suresh, 1989) or a full three-dimensional model (Levy and Papazian, 1990; Hom, 1992). The plane strain model actually represents fibres and produces conservative values. The plane stress case represents a thin plate with reinforcement "plugs". The axisymmetric model has been used in a number of investigations to analyze reinforcement-matrix reactions. However, since it is a volume of revolution, there is some difficulty accounting for the entire matrix and boundary conditions. One is also limited to specific inclusion geometries and only uniaxial and thermal expansion cases can be investigated.

The three dimension analysis is more complicated and more numerically intensive

than the options given above, however, the available reinforcement shapes and load conditions which can be studied are unlimited. Such a model is no longer beyond the capabilities of a reasonable computer work station and has become popular for the analysis of discontinuous metal matrix composites.

The unit cell approach is not strictly limited to the cases defined above. The aspect ratios of the unit cell and inclusion do not have to be one and can be applied to the study of whisker reinforced composites. It can also be adapted to study such variables as particle clusters and orientation. The simple model used in this investigation, however, is suitable for studying the effects of volume fraction of reinforcement, particle shape, residual thermal stresses, various external loads and changes in the composite material properties.

2.2.2   Boundary Conditions

An important consideration is the boundary conditions to be applied to the unit cell. First, however, the problem is further reduced by considering the symmetry of the unit cell. The unit cells considered in this analysis are cube shaped and contain either cubical or spherical particles, therefore only one sixteenth of the three dimension unit cell must be considered. However, to keep the geometry and application of boundary conditions simple, one eighth of the unit cell, as shown in Figure 2.4, will be used for all loading conditions.

Boundary conditions must be applied to this reduced model to enforce the periodicity of the original composite structure. The reduced unit cell is defined by the

following six plane: $S(x_1=0)$, $S(x_2=0)$, $S(x_3=0)$, $S(x_1=l_1)$, $S(x_2=l_2)$ and $S(x_3=l_3)$. The first three are the planes of symmetry, and therefore, there must not be any normal displacement, only translation along the surface is allowed. A condition of the periodic structure is that the free surfaces must remain flat with the same orientation after a displacement occurs. This is illustrated in Figure 2.5. The six sides of the unit cell are constrained according to

$$
\begin{aligned}
U_{S(x_1=0)} &= 0 \\
U_{S(x_2=0)} &= 0 \\
U_{S(x_3=0)} &= 0 \\
U_{S(x_1=l_1)} &= u_1 \\
U_{S(x_2=l_2)} &= u_2 \\
U_{S(x_3=l_3)} &= u_3
\end{aligned}
\qquad (2.25)
$$

The values of u_1, u_2 and u_3 are defined in the following section.

2.2.3   Application of External Loads

External loads may be imposed on the finite element model by prescribing displacements or forces to the nodes. These may be applied to produce a constant displacement or constant pressure over a surface.

The loading procedures in the thermal residual stress analyses were set to model the processing of the composite and then loading. As such, the composite was cooled from a processing temperature of 500°C to room temperature, 20°C. External loads were then applied as surface pressures, while the boundary conditions requiring the surfaces to remain plane were still in effect. During the temperature drop, the temperature was

25

the same throughout the unit cell.

In ADINA, the loads were applied by prescribed displacements. Each node on the surface was moved the same distance normal to the surface. This automatically imposes the boundary condition that the surface remain a flat plane with the same orientation. Under a uniaxial load, the displacement u_1, in Eq. 2.25, was prescribed. If a biaxial load was applied, then u_1 and u_2 were prescribed.

2.2.4 Mesh Generation and Verification

All element meshes were generated in the ANSYS preprocessor and were then converted to the ADINA format if required. This basically consisted of rearranging the order of the nodes in the element connectivity. For convenience, all models were built using eight node isotropic three-dimensional solid elements containing eight Gaussian integration points each. For this small displacement analysis rotations were omitted and each node had three degrees of freedom.

For each unit cell, one with a spherical inclusion and one with a cube shaped reinforcement, three different meshes of varying densities were tested. Each mesh had approximately twice as many degrees of freedom as the previous model. The resulting uniaxial stress-strain curves for each reinforcement geometry were compared. It was found that the medium and fine meshes produced similar results, however, the coarse mesh produced higher stresses under plastic deformation. In the interest of computation time, the medium mesh was used in each case, the resulting meshes are shown for a spherical inclusion in Figure 2.6 and a cube inclusion in Figure 2.7. The model for the

26

spherical reinforcement has 1613 nodes and 1296 elements and there are 2744 nodes and 2197 elements in the cube inclusion model.

2.2.5   The Elastic Reinforcement

It has become a popular procedure to model the reinforcement phase as a purely elastic isotropic material. Since the strength of Alumina fibres is in the range of 1300 to 2100 MPa, it is unlikely that it will experience these stresses in a normal use of the composite and failure is not considered in the model.

An isotropic elastic material will respond according to Hooke's law:

$$\epsilon_{xx} = \frac{1}{E}[\sigma_{xx} - \nu(\sigma_{yy} + \sigma_{zz})] + kT$$

$$\epsilon_{yy} = \frac{1}{E}[\sigma_{yy} - \nu(\sigma_{xx} + \sigma_{zz})] + kT$$

$$\epsilon_{zz} = \frac{1}{E}[\sigma_{zz} - \nu(\sigma_{xx} + \sigma_{yy})] + kT \qquad (2.26)$$

$$\epsilon_{xy} = \frac{(1+\nu)}{E}\sigma_{xy} \qquad \epsilon_{yz} = \frac{(1+\nu)}{E}\sigma_{yz} \qquad \epsilon_{zx} = \frac{(1+\nu)}{E}\sigma_{zx}$$

where kT is the term related to thermal expansion.

In this investigation, the reinforcement has been assigned the following properties.

E = 450 000 MPa

ν = 0.25

k = $8 \times 10^{-6}/^{\circ}C$

These values are similar to those used by other researchers in similar studies.

Previous investigations have shown that large Al_2O_3 particles often contain flaws and may fail when the composite experiences large strains (Lloyd, 1991; Bao, 1992;

27

Mochida, Taya and Lloyd, 1991), but this is not considered in the present analysis. The unit cell approach represents the average of a random distribution of particles, therefore the reinforcement is considered an isotropic material although the properties of alumina are dependent on the crystal structure.

2.2.6 The Kinematic Hardening Elastic-Plastic Matrix

The matrix material model, used in the residual thermal stress analysis in the ANSYS code, was a rate independent multilinear kinematic hardening elastoplastic model. In this model, the size of the yield surface does not change but the centre of the surface moves. This is shown in Figure 2.8.

The kinematic hardening model is based on an incremental procedure in which each strain increment can be divided into its elastic and plastic parts.

$$d\epsilon_{ij} = d\epsilon_{ij}^e + d\epsilon_{ij}^p \tag{2.27}$$

The elastic part is described by the Hooke's law and the plastic strain increment is found by using the flow law:

$$d\epsilon_{ij}^e = \frac{1}{E}[(1+v)\delta_{ik}\delta_{jl} - v\delta_{ij}\delta_{kl}]d\sigma_{kl}$$

$$d\epsilon_{ij}^p = \lambda \frac{\partial f(\sigma)}{\partial \sigma_{ij}} \tag{2.28}$$

Where δ_{ij} is the Kronecker delta, λ is a scalar function and the yield surface is defined by

in which q is the radius of the yield surface and $f(\sigma,\alpha,\varkappa)$ is the yield function. When the

28

$$\Phi = f(\sigma,\alpha,\chi) - q^2 = 0 \tag{2.29}$$

yield function is equal to the plastic potential, it is termed the associative flow rule and the plastic strains act in the direction normal to the yield surface. The variables are defined as α, the location of the centre of the yield surface and χ is the plastic work,

$$\alpha_{ij} = \int C d\epsilon_{ij}^p$$
$$\chi = \int (\sigma_{ij})^T d\epsilon_{ij}^p \tag{2.30}$$

where C is a constant and T indicates the transpose of the tensor. The plastic potential function can be differentiated to give

$$df = \left(\frac{\partial f}{\partial \sigma_{ij}}\right)^T d\sigma_{ij} + \left(\frac{\partial f}{\partial \chi}\right) d\chi + \left(\frac{\partial f}{\partial \alpha_{ij}}\right) d\alpha_{ij} = 0 \tag{2.31}$$

substituting

$$d\alpha_{ij} = C d\epsilon_{ij}^p \tag{2.32}$$

and

$$d\chi = (\sigma_{ij})^T d\epsilon_{ij}^p \tag{2.33}$$

gives

$$\left(\frac{\partial f}{\partial \sigma_{ij}}\right)^T d\sigma_{ij} + \left(\frac{\partial f}{\partial \chi}\right)(\sigma_{ij})^T d\epsilon_{ij}^p + \left(\frac{\partial f}{\partial \alpha_{ij}}\right)^T C d\epsilon_{ij}^p = 0 \tag{2.34}$$

The stress increment is calculated using the elastic stress-strain relation,

$$do_{ij} = D_{ij} d\epsilon_{ij}^e \qquad (2.35)$$

where **[D]** is the elastic stiffness matrix and the elastic strain increment is determined from

$$d\epsilon_{ij}^e = d\epsilon_{ij} - d\epsilon_{ij}^p \qquad (2.36)$$

Combining Eqs. 2.34, 2.35 and 2.36 leads to

$$\lambda = \frac{\left(\dfrac{\partial f}{\partial \sigma_{ij}}\right)^T D_{ij} d\epsilon_{ij}}{-\dfrac{\partial f}{\partial \chi}(\sigma_{ij})^T \dfrac{\partial f}{\partial \sigma_{ij}} - C\left(\dfrac{\partial f}{\partial \alpha_{ij}}\right)^T \dfrac{\partial f}{\partial \sigma_{ij}} + \left(\dfrac{\partial f}{\partial \sigma_{ij}}\right)^T D_{ij} \dfrac{\partial f}{\partial \sigma_{ij}}} \qquad (2.37)$$

and the plastic strain increment is then calculated using Eq. 2.28. A description of the full application of this constitutive relation is provided in the ANSYS Theory Manual (1992).

For use as a temperature dependent material model, a thermal strain increment is added which is dependent on the change of temperature. The model is rate independent therefore no creep or relaxation is included in the analysis.

This model is adequate for simple monotonic loads but does not describe the material behaviour under cyclic or nonproportional loads. It does not account for the hardening which occurs under a constant strain amplitude cyclic load or the extra hardening associated with a nonproportional loading. The addition of the reinforcing material produces these nonproportional stresses within the matrix of a metal matrix composite. The following section briefly describes the Ellyin and Xia constitutive relation which accounts for these effects.

2.2.7 The Ellyin and Xia Model for an Elastic-Plastic Matrix

In ADINA, the behaviour of the aluminum matrix was determined by a material model based on the rate independent two surface constitutive relation developed by Ellyin and Xia. This method is applicable to multiaxial nonproportional cyclic loads but require only a few extra input parameters. A complete description and derivation of the constitutive relation can be found in (Ellyin, 1989; Ellyin and Xia, 1989; Xia and Ellyin, 1991). Examples of this model applied to two dimensional plane strain finite element analysis can be found in (Ellyin and Wu, 1992; Wu, 1989).

The yield surface, which defines the boundary between elastic and plastic loading is given by

$$\phi_y = f_y(\sigma_{ij}-\alpha_{ij})-q^2 = 0 \tag{2.38}$$

where α_{ij} is the location of the centre of the yield surface and the variable q is the radius and is a function of accumulated plastic strain,

$$l_p = \int \left(\frac{2}{3}d\epsilon^p_{ij}d\epsilon^p_{ij}\right)^{\frac{1}{2}} \tag{2.39}$$

The second surface is the stress memory surface given by

$$\phi_m = f_m(\sigma_{ij}-\beta_{ij})-R^2(\sigma_{eq,max}) = 0 \tag{2.41}$$

In this case β_{ij} is the centre of the memory surface, R is the radius and $\sigma_{eq} = (3s_{ij}s_{ij}/2)^{1/2}$ where $s_{ij} = \sigma_{ij}-\sigma_{kk}\delta_{ij}/3$. The stress memory surface records the load history of the material by memorizing the maximum equivalent stress experienced. For a von Mises material,

these surfaces become:

$$f_y = \frac{3}{2}(s_{ij}^\alpha s_{ij}^\alpha)$$

$$f_m = \frac{3}{2}(s_{ij}^\beta s_{ij}^\beta)$$

(2.41)

Where the s_{ij}^α is the deviatoric part of $\sigma_{ij}-\alpha_{ij}$ and s_{ij}^β is the deviatoric part of $\sigma_{ij}-\beta_{ij}$.

The total strain increment is expressed as the sum of the elastic and plastic parts,

$$d\epsilon_{ij} = d\epsilon_{ij}^e + d\epsilon_{ij}^p$$

(2.42)

The stress increments are then determined using the Hooke's law for the elastic part and the increment of plastic strain is given by

$$d\epsilon_{ij}^p = cg\frac{\partial f_y}{\partial \sigma_{ij}}\frac{\partial f_y}{\partial \sigma_{kl}}d\sigma_{kl}$$

(2.43)

The total stress increment is then

$$d\sigma_{ij} = \frac{E}{1+v}\left(\delta_{ik}\delta_{jl}+\frac{v}{1-2v}\delta_{ij}\delta_{kl}\right)d\epsilon_{kl}$$

$$-\frac{E}{1+v}\left\{\frac{cg\frac{\partial f_y}{\partial \sigma_{ij}}}{\frac{1+v}{E}+cg\left(\frac{\partial f_y}{\partial \sigma_{mn}}\frac{\partial f_y}{\partial \sigma_{mn}}\right)}\left(\frac{\partial f_y}{\partial \sigma_{kl}}+\frac{v}{1-2v}\frac{\partial f_y}{\partial \sigma_{pp}}\delta_{kl}\right)\right\}d\epsilon_{kl}$$

(2.44)

In the above, δ_{ij} is the Kronecker delta and c is defined according to whether it is an elastic or plastic state of stress, i.e:

32

$$c = 1 : \frac{\partial f_y}{\partial \sigma_{kl}} \sigma_{kl} \geq 0 \; \wedge \; f_y(\sigma_{ij} - \alpha_{ij}) - q^2 = 0$$

$$c = 0 : \frac{\partial f_y}{\partial \sigma_{kl}} \sigma_{kl} < 0 \; \vee \; f_y(\sigma_{ij} - \alpha_{ij}) - q^2 < 0$$

(2.45)

The variable g, is the hardening modulus, and is given by

$$g = \frac{1}{4q^2} \left(\frac{1}{E_t} - \frac{1}{E} \right)$$

(2.46)

where E is the elastic modulus and E_t is the tangent modulus.

To determine the movement of the yield and stress memory surfaces and the tangent modulus, two different modes of plastic loading are defined. The first is monotonic plastic loading (ML). In this case, the stress memory surface expands with the movement of the yield surface and the two surfaces remain tangent. This is shown by path AB in Figure 2.9. The second mode is plastic reloading (RL) in which the yield surface moves inside the stress memory surface as shown by path CD. If the yield surface contacts the memory surface, the maximum equivalent stress increases once again and returns to monotonic plastic loading.

A Ziegler type rule is used to determine the motion of the yield surface under monotonic plastic loading. The movement is then a function of stress and the current position and a scalar function $d\mu$.

$$d\alpha_{ij} = d\mu(\sigma_{ij} - \alpha_{ij})$$

(2.47)

When plastic reloading occurs, the yield surface moves in the direction of the line connecting the points (points D and E, see Figure 2.9) on the yield and memory surfaces

33

having the same normal vector. This is described by:

$$da_{ij} = d\mu(\sigma_{ij}^m - \sigma_{ij}^y) \qquad (2.48)$$

Using the consistency condition

$$d\phi_y = \frac{\partial f_y}{\partial \sigma_{ij}}(d\sigma_{ij} - d\alpha_{ij}) - 2qdq = 0 \qquad (2.59)$$

α_{ij} can be determined for either of the above two cases.

The evolution of the stress memory condition is also dependent on the two types of plastic loading. For the monotonic plastic loading, the movement of the memory surface is determined by the condition that the yield and memory surfaces must remain tangent. This is enforced by the following condition (Ellyin, 1989):

$$\frac{\partial f_y(\sigma_{ij} - \alpha_{ij})}{\partial \sigma_{ij}} = \lambda \frac{\partial f_m(\sigma_{ij} - \beta_{ij})}{\partial \sigma_{ij}} \qquad (2.50)$$
$$f_m(\sigma_{ij} - \beta_{ij}) = R^2$$

When plastic reloading occurs, the movement of the stress memory surface is found using the accumulated plastic strain, l_p, in

$$\frac{\partial \beta_{ij}}{\partial l_p} = K_2(\sigma_{ij}^{mean} - \beta_{ij}) \qquad (2.51)$$

where σ_{ij}^{mean} is the geometric centre of the cyclic stress path.

The method of determining the tangent modulus, E_t, is also dependent on the type of plastic loading. For the monotonic plastic loading, E_t is treated as a function of equivalent stress and is found using an equation of the form:

34

$$E_t = f(\sigma_{eq})$$
(2.5)

In the case of plastic reloading, the tangent modulus is dependent on the ratio of the lengths of lines CD (δ_2) and DE (δ_1) in Figure 2.9. The functional form is

$$E_t = E_t(\sigma_{eff}, r)$$
(2.53)

where

$$r = \frac{\delta_1}{\delta_2} = \frac{d_1}{d_2} .$$
(2.54)

Thus, when the stress is located at C (the onset of plastic reloading), $\delta_2 = 0$, $r = \infty$ and $E_t = E$. When the stress reaches the memory surface and returns to the monotonic plastic loading $\delta_1 = 0$, $r = 0$ and $E_t = E_{t,\sigma max}$. The ratio r determines a unique point on the effective stress-strain curve at which the tangent modulus is taken, as shown in Figure 2.10.

Transient hardening or softening of the material is accounted for by a change in size of the yield surface and a change in the tangent modulus. Both of these modifications are a function of the accumulated plastic strain. Hardening in the tangent modulus is bounded by the monotonic and master curves. The equivalent stress-strain is taken as one of the family of curves defined by

$$E_t = E_{ts} - (E_{ts} - E_{t0})e^{-\gamma l_p}$$
(2.55)

where E_{t0} is the tangent modulus on the monotonic stress-strain relation, and E_{ts} is the modulus from the saturated stress-strain curve. The scalar γ, is a material property which describes how fast the material reaches a saturation state. Transient hardening is also

reflected in the growth of the yield surface by

$$q = q_s - (q_s - q_o)e^{-\gamma l_p}$$
(2.56)

In the above equation q_s is the radius of the stable yield surface and may be a function of the maximum effective strain.

This constitutive relation has been tested for numerous materials under various load conditions and has been found to be far more accurate than the conventional isotropic or kinematic hardening models, e.g. see Xia, Ellyin and Wu (1995).
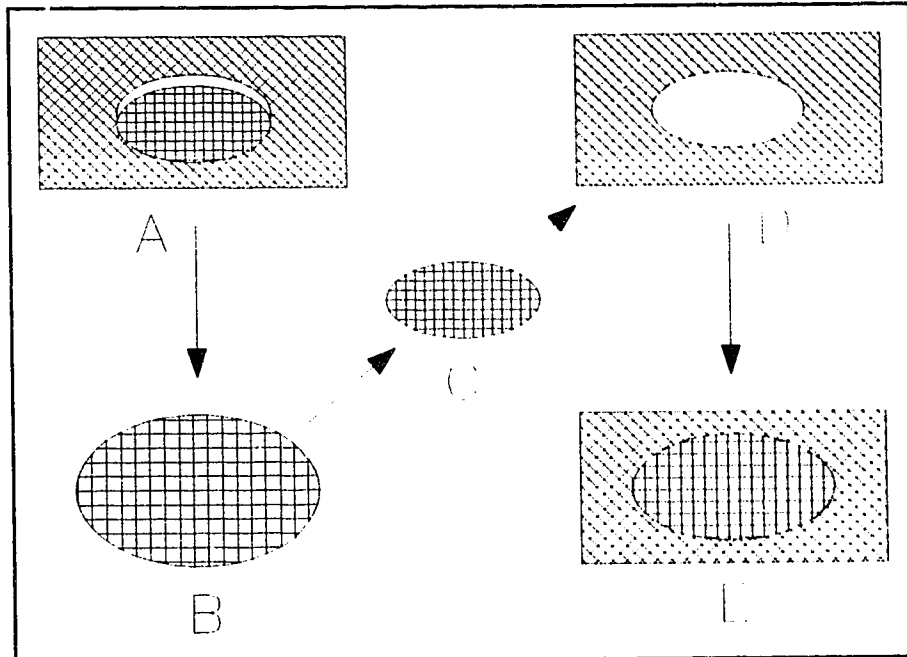
Figure 2.1: The Eshelby cutting and welding procedure.
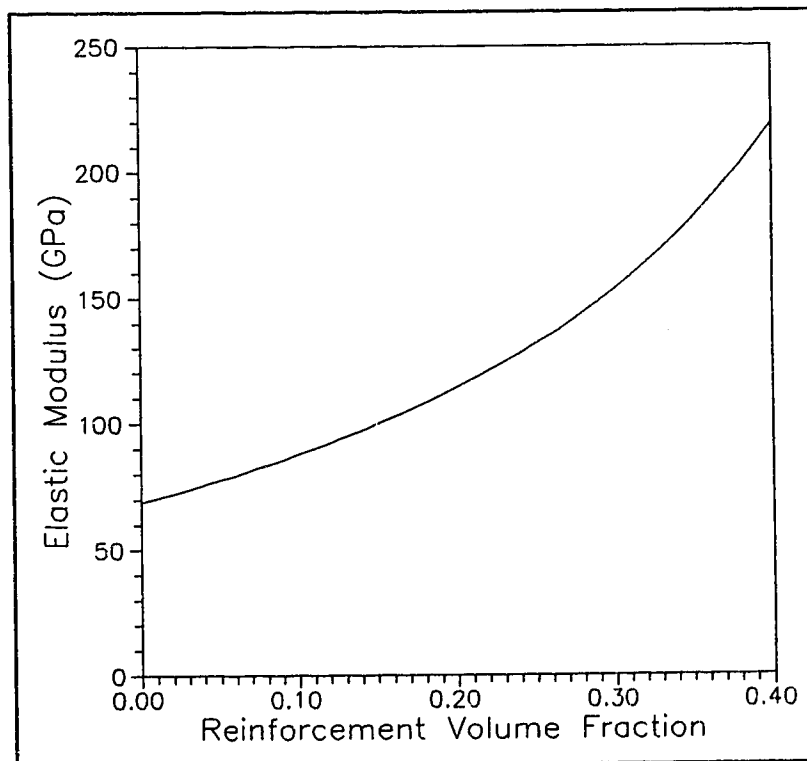
Figure 2.2: Results from Eshelby calculation for aluminum (E=69500 MPa) and Al_2O_3 (E=450000 MPa)
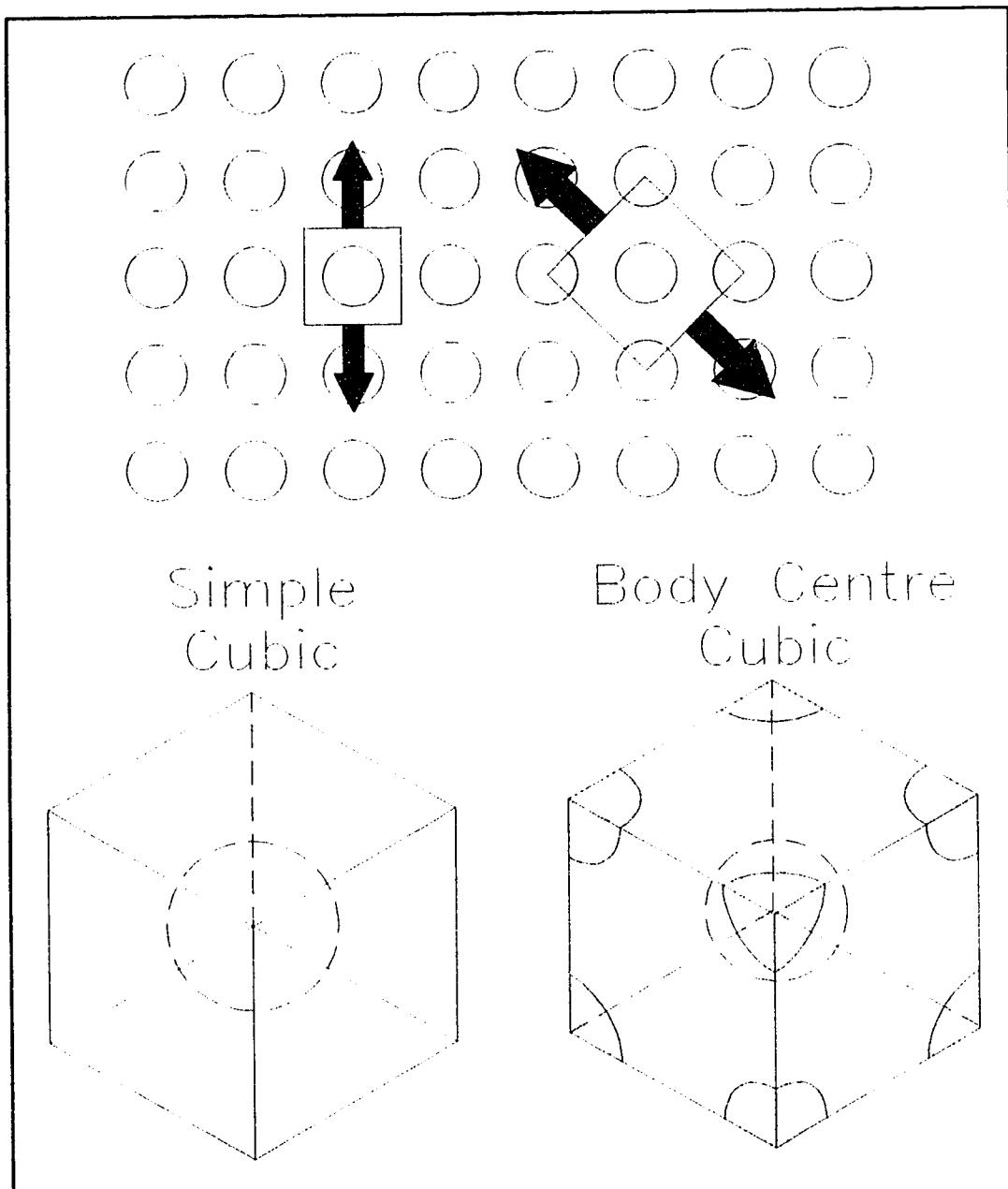
Figure 2.3: The simple cubic and body centre cubic unit cells.
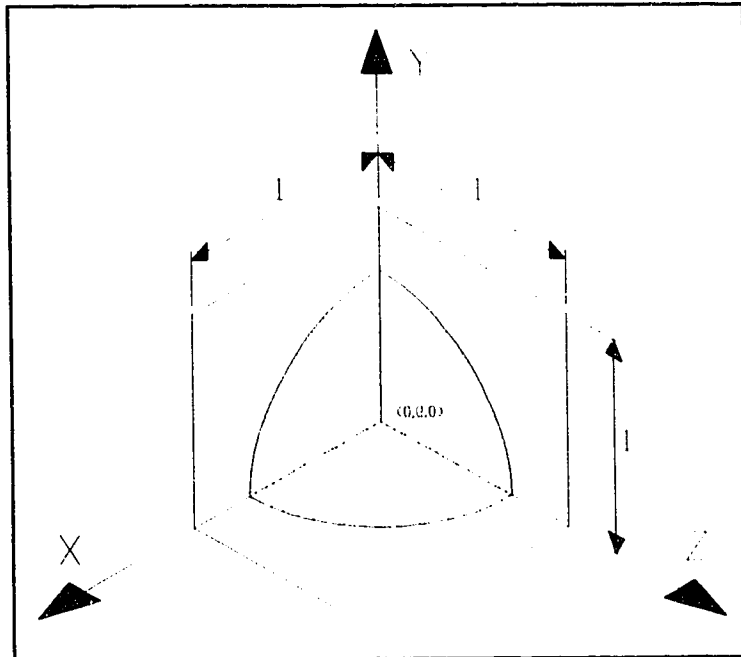
Figure 2.4: One eighth of the unit cell is used for the finite element model.
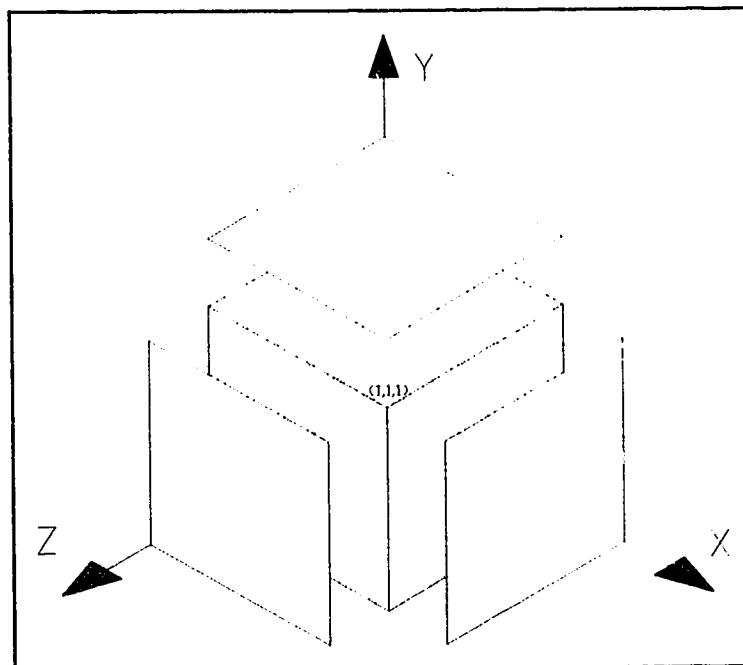
Figure 2.5: Boundary conditions on the finite element model.
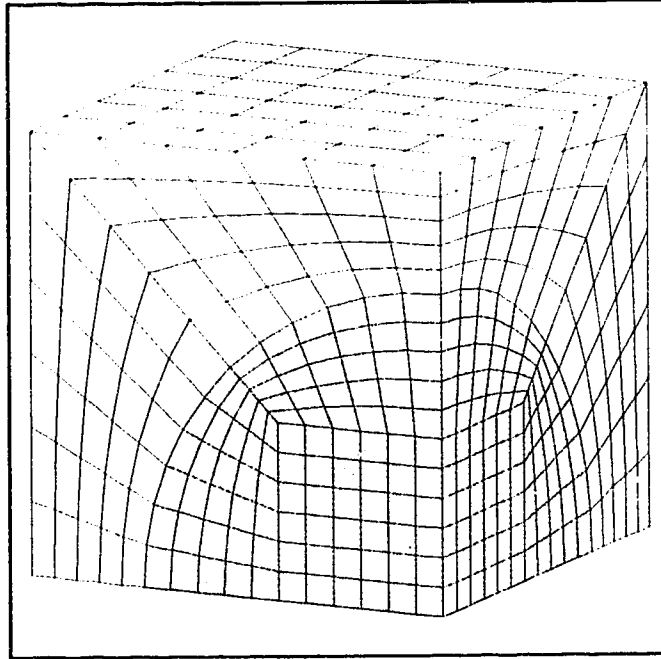
Figure 2.6: The finite element mesh for the unit cell containing a spherical inclusion.
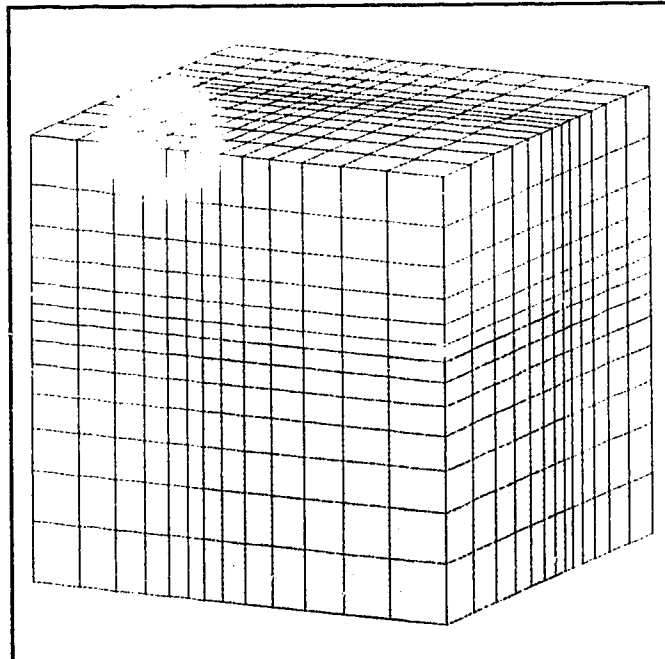
Figure 2.7: The mesh used for the unit cell containing cube shaped inclusion.
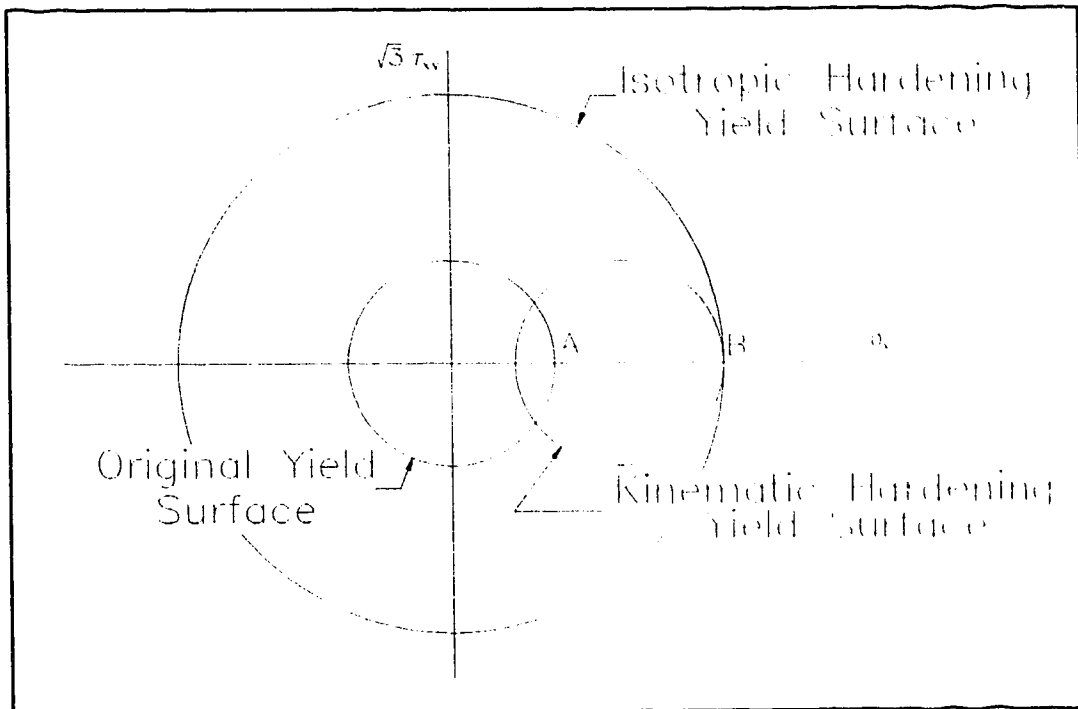
Figure 2.8: The isotropic and kinematic hardening yield surfaces.
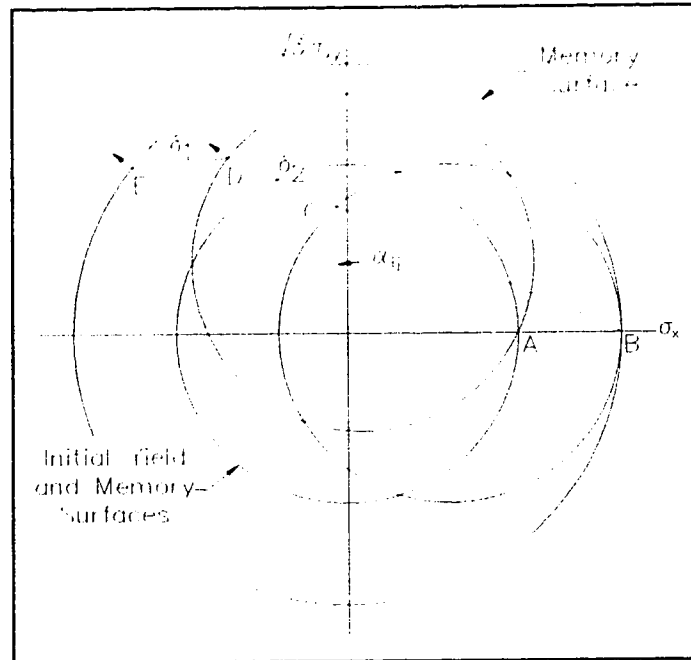
Figure 2.9: Movement of the yield surface in the Ellyin and Xia constitutive relation.
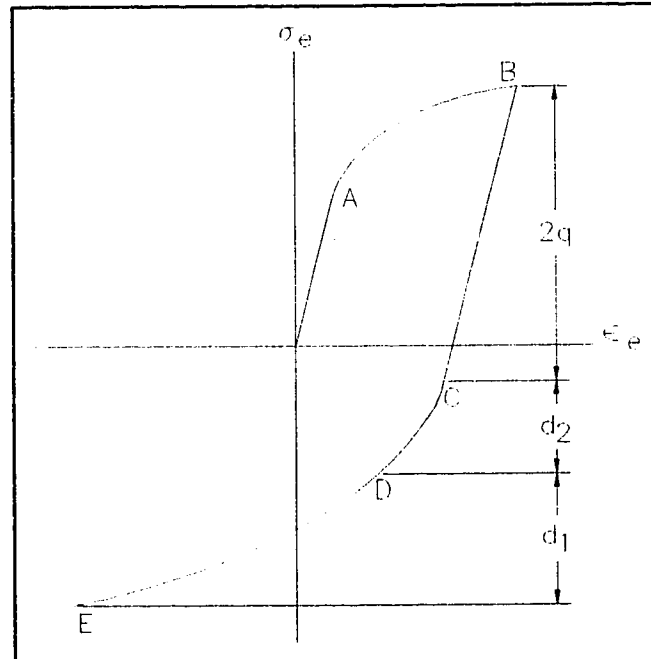
Figure 2.10: Determination of the current tangent modulus from the movement of the yield surface in the Ellyin and Xia material model.

42

3 Comparison of Results from Experimental and Numerical Analyses

3.1 Description of Biaxial Tests

Tubular specimens of 6061 and 20% Al_2O_3p 6061 were tested using the multiaxial testing apparatus described below. A wide range of tests was conducted to determine the properties of the matrix materials to be used in the finite element analysis and examine the behaviour of the composite under complex loads. The complete testing program is described in Section 3.1.3.

3.1.1 The Biaxial Testing Machine

All tests were completed using the biaxial testing machine located in the materials laboratory of the Department of Mechanical Engineering at the University of Alberta. This machine is a MTS system modified to apply an additional internal/external pressure differential to tubular specimens. The apparatus, shown in figure 3.1, consists of a MTS system capable of applying a 10 000 lbs axial load with a pressure vessel mounted around the hydraulic ram, specimen,load cell and load frame. A constant pressure, up to 3 000 psi, is applied in the pressure vessel around the exterior of the specimen while a variable pressure, 0 to 6 000 psi, is applied to the interior of the specimen. This allows for a positive and negative pressure difference, and therefore a fully reversed cyclic loading can be applied. In this design, the load cell is contained within the pressure vessel; the load cell sensitivity to pressure must be taken into account, but the need for low friction seals is eliminated.

43

The specimen strain is measured by two specially constructed extensometers, one measures the change in diameter, while the other measures the change in axial gauge length. These extensometers are held on the specimen using springs and are placed over patches on the specimen so the knife edges do not contact and damage the specimen.

The test is controlled by a personal computer and may be programmed for any number of specific load conditions. The computer generates the command signals for each channel which the axial and diametral strains are forced to follow under strain control mode. The command signals may be of any shape, i.e. ramp, sinusoidal or triangle and the two channels may be in or out of phase. The computer also records four channels of data: axial load, axial strain, internal pressure and diametral strain. Given that the external pressure is constant, the stresses within the specimen can be calculated from the following equations:

$$\sigma_a = \frac{F}{A}$$

$$\sigma_t = (p_i - p_e) \frac{D_e + D_i}{2(D_e - D_i)} \tag{3.1}$$

$$\sigma_r \approx \frac{-(p_i + p_e)}{2}$$

Where F is the effective applied axial load, A is the cross sectional area of the specimen, p_i and p_e are the internal and external pressures and D_i and D_e are the internal and external diameters of the specimen.

Most tests results reported in the literature available are for uniaxial monotonic or cyclic loads. No multiaxial results, other than those from this facility (Ellyin, Xia and

44

Meijer, 1993) have been found for discontinuous metal matrix composites. Usually when biaxial tests are conducted, they are a combination of uniaxial and torsional loads. The range of biaxial strain paths for these loads are shown in Figure 3.2. The biaxial testing machine described above has the unique ability to produce any strain path on the plane shown in Figure 3.2.

3.1.2 Specimen Geometry

Thin walled tubular specimens are used in 'c' pparatus described above. The specimen shown in Figure 3.3 was designed to provide a large gauge length but allow for high strains and plastic deformation. This geometry has been used previously and does not result in significant bending stresses in the specimen. This geometry has been found to be useful for small cyclic strains, however the thin gauge section will buckle under large compressive loads. For this reason, strain amplitudes are limited and for materials with high yield stresses the amount of plastic deformation which can be produced is small.

3.1.3 The Material Testing Program

The experimental analysis can be divided into two separate sections; tests on the aluminum alloys and tests on the composites.

The investigation into the behaviour of 6061-T0 and 6061-T6 materials was conducted to determine the material properties to be used in the finite element analysis. The tests conducted were:

- monotonic uniaxial load

- uniaxial cyclic step test.

The uniaxial cyclic step test contained numerous short tests of 100 cycles at each step with strain amplitudes from the elastic limit to the point where the specimen buckled. All tests were done under strain control mode. Cyclic tests were completed using a frequency of 0.125 Hz. This speed was selected after tests done on 6061-T6 at 0.0025, 0.025 and 0.125 Hz produced similar results indicating the matrix materials are rate independent.

The test program for the 20% Al_2O_3p 6061 was designed to illustrate the behaviour of the composites under simple and complex loads. These results were also required to compare to those from the numerical analysis to show the accuracy of the model.

The tests conducted on the composites in the T0 and T6 conditions were:

- monotonic uniaxial load

- uniaxial cyclic load

- uniaxial cyclic step test

- equibiaxial cyclic load

- 90° out of phase biaxial cyclic load.

The experimental and numerical results are compared in Section 3.3.

3.2   Numerical Simulations of Composite Behaviour

Numerical analysis of the composite was completed using the simple three dimensional body centre cubic unit cell model. The discetized unit cell and the boundary

conditions applied are as described in Eq. (2.25) in the second chapter. The resulting average stress and strain within the model was found by summing the reactions on the constrained surfaces and from the displacement of the nodes on the loaded surfaces. Most load conditions were applied to the unit cell with a spherical inclusion. For the sake of comparison, simulations of monotonic loading were also completed on unit cells containing cube shaped particles. The strain step size selected varied for each material, load type and load amplitude, however, all were selected to give sufficient data points and quick convergence. Actual numerical solution times also varied, but were significantly longer for the case of the cube inclusion which requires a greater mesh density due to the high stress concentration.

3.2.1   Verification of the Ellyin and Xia Elastoplastic Matrix Material Model

The use of the Ellyin and Xia constitutive relation to model the elastoplastic matrix requires the plastic portions of the initial monotonic and stable stress-strain curves and a strain hardening parameter. Both of the interpolation curves were found by performing tests on the matrix materials 6061 aluminum in the T0 and T6 heat treatments. The hardening parameter, γ, can be approximated from a uniaxial cyclic test by estimating the accumulated plastic strain. The finite element analysis of the matrix material requires only one eight node element since it involves uniform stress and strain distributions.

3.2.1.1 Uniaxial Monotonic Load Verification

The results of the uniaxial monotonic load on the finite element model and the test specimens are shown in Figure 3.4. The numerical stress-strain curve matches the input data exactly as it should. The monotonic interpolation curves were taken directly from the test data starting at the yield point and ending at the maximum test strain. Sixteen data points were taken at increasing interval sizes; the last strain increment being 20 times the first. This was done to place more interpolation points where the rate of change in slope is the greatest. For both the T0 and T6 heat treatments, the elastic modulus was $E = 69\ 500$ MPa and the Poisson's ratio was $v = 0.33$. The initial monotonic proportional limits applied were $\sigma_y = 34$ MPa for 6061-T0 and $\sigma_y = 264$ MPa for 6061-T6.

3.2.1.2 Uniaxial Cyclic Load Verification

Uniaxial cyclic tests were also done for each of the aluminum matrices and the results are shown in Figures 3.5 and 3.6. Cyclic numerical tests require extra interpolation data for the stable curve. Data for these curves was required over the same range, starting from the proportional limit, at the same spacing. Since the range of the cyclic step tests completed was not as large as the monotonic tests (due to the specimen being unable to handle large compressive strains without buckling) the stable curve was assumed to run parallel to the monotonic curve for the data that was not available. The results of the cyclic step tests on the aluminum specimens are provided in Appendix C.

Another consideration of the cyclic behaviour is the change in proportional limit

with increasing strain amplitudes. In a Masing type material, the yield strength remains constant at various strain amplitudes. The annealed 6061 is clearly not a Masing material, and the subroutine was modified to account for the change in yield point according to:

$$if \ \epsilon_{eqv,max} < 0.005 \ then \ q_s = 34-192.67\epsilon_{eqv,max}+378535\epsilon^2_{eqv,max} \qquad (3.2)$$
$$if \ \epsilon_{eqv,max} \geq 0.005 \ then \ q_s = 42.50 MPa$$

This was found from the cyclic step test data provided in Appendix C. The T6 heat treated aluminum was also a non-Masing material. The proportional limit found from monotonic loading is 264 MPa and appears to rapidly change to an asymptotic value of 154 MPa as the strain amplitude was increased. In other words, a small amount of cyclic softening was observed during the first few cycles on the T6 heat treated aluminum alloy. In the subroutine the proportional limit of the T6 treated aluminum was decided by

$$if \ \epsilon_{eqv,max} < 0.0038 \ then \ q_s = 264 MPa$$
$$if \ \epsilon_{eqv,max} \geq 0.0038 \ then \ q_s = 154 MPa \qquad (3.3)$$

The interpolation values for the stable stress-strain curves of the two matrix materials are shown in Figure 3.4.

Another parameter which had to be defined in this cyclic loading test was the rate of hardening (γ in Eqs. (2.56) and (2.57)). Although γ can be calculated using an estimate of the accumulated plastic strain, this was essentially a trial and error process. Both the T0 and T6 treated material stabilize rapidly, so large values of γ were expected. A value of $\gamma = 256$ was found to be suitable for 6061-T0 while for the 6061-T6 a value of $\gamma = 1000$ was used since it stabilises almost immediately after the first load reversal.

The numerical results for both materials show close agreement with the

experimental results. In both cases, the hardening of the materials differ slightly between the experimental and numerical results, but this deviation is within experimental variation.

3.3 Comparison of Predicted Composite Properties with Experimental Results

In this section, the experimental results from tests done on the 20% Al_2O_3 6061 composite will be compared with the numerical results. For multiaxial loads, the stress-strain curves are provided for the axial and hoop directions. Where available, the results on the 6061 alloy are also given.

3.3.1 Uniaxial Monotonic Load Results

The monotonic load tests were done by applying an axial load to the tubular specimens. No internal or external pressures were applied. Figure 3.7 shows the uniaxial stress-strain relation for 6061 aluminum and 20% Al_2O_3p 6061 in the T0 and T6 conditions. The values for proportional limit, 0.2% offset yield strength and elastic modulus are provided in table 3.1. It is very difficult to determine the proportional limit of the composite in the T0 condition since it exhibits nonlinear behaviour starting almost immediately after the external load is applied (see figure 3.7). For this reason, the elastic modulus of this composite was taken from the first load reversal of the uniaxial cyclic test.

Table 3.1: Material properties recorded from experimental and numerical analysis on composites and matrix materials alone.

Material (Analysis and Inclusion Shape)		Elastic Modulus E (MPa)	Proportional Limit σ_y (MPa)	0.2% Yield Stress $\sigma_{y(0.2\%)}$ (MPa)
6061-T0		69500	34	68
20% Al$_2$O$_3$ 6061-T0 (Experimental)		74000	20	76
20% Al$_2$O$_3$ 6061-T0 (Numerical)	Sphere	102000	40	87
	Cube	102000	40	103
6061-T6		69500	264	320
20% Al$_2$O$_3$ 6061-T6 (Experimental)		106700	185	365
20% Al$_2$O$_3$ 6061-T6 (Numerical)	Sphere	102000	190	359
	Cube	102000	220	403

As expected, the experimental strength and elastic modulus of the composite are greater than the values for aluminum alloy for each heat treatment. However, the proportional limits are lower for the composite. For example, the annealed aluminum specimen has a proportional limit of 35 MPa when the value is only 20 MPa for the composite. The specimens in the T6 condition produced proportional limits of 264 MPa and 185 MPa for the aluminum alloy and composite respectively. The lower proportional limit is caused by residual thermal stresses in the composite due to the difference in the coefficients of expansion for the matrix and the reinforcement. In this case, the residual stresses are large enough for the composite to show nonlinear behaviour at very small external loads. A detailed analysis of the thermal residual stresses is provided in Chapter four. Another reason for this behaviour is the stress concentrations which occur in the matrix near the particle. This results in confined zones of plasticity in the composite at global stresses that are lower than the yield stress of the matrix.

In each heat treatment, the composite has a much higher 0.2% offset yield stress than the aluminum alloy. This is due to the increased initial hardening rate within the composite. This hardening results in the composite having a much greater 0.2% offset yield than the aluminum even though the proportional limit of the composite is much lower. While the initial increase in strength is large, when the composite experiences large plastic deformations the slope of the stress-strain curve becomes very close to that of the aluminum alloys.

Significant differences due to reinforcement shape can also be noted. For each condition of heat treatment the cube inclusion produces much higher initial hardening.

52

This can be explained by the stress distribution around the reinforcement. In the case of the cube inclusion there are small regions of very high stress concentration at the edges and corner of the particle. Although the stresses are very high in these areas, the rest of the matrix remains elastic. On the other hand, the stresses around a sphere inclusion are much lower but are spread out ᵥ er a much larger zone. This reduces the effect of load transfer to the reinforcement. This leads one to the conclusion that as the composite strain becomes larger and more of the matrix is deforming plastically, the two curves for spherical and cube inclusions should become parallel which, in fact, they do. For the T0 condition composite this occurs at a strain ⁻ ⁻ %. This is quite evident in Figure 3.8 which shows the axial and hoop stress-strain responses under equibiaxial load. Saturation occurs more quickly under equibiaxial loads because of equivalent strains produced are much higher.

3.3.2   Uniaxial Cyclic Tests

The uniaxial cyclic tests were conducted in a manner similar to the uniaxial monotonic experiments. The axial strain was forced to follow a sawtooth signal resulting in the strain controlled cyclic load. This test involves compressive loads, therefore the strain range was limited by the buckling of the specimen.

These tests showed the same trends; i.e. greater strength and stiffness in the composite compared to the matrix alloy. The results for the T0 and T6 treated specimens are shown in Figures 3.9 and 3.10, respectively. The dashed lines show the experimental results from similar tests conducted on the aluminum alloy on its own.

The hysteresis loops for the annealed specimens, shown in Figure 3.9, show a large amount of plasticity which is defined by the width of the loops. An important feature to note is how quickly the composite and aluminum stabilize after significant hardening in the first cycle. The annealed materials stabilize within ten cycles. Once again the composites appear to reflect the properties of the matrix material. The composite hysteresis loops also appear to be symmetric; i.e. the positive and negative stress amplitudes are about equal.

Upon comparison of the numerical and experimental results, one observes very good agreement, despite using a very simple model containing a spherical inclusion. Discrepancies, however, can be seen in the monotonic portion of the load and the hardening rate. In the plot of the numerical results, the monotonic stress values are clearly larger than the experimental values. This is likely due to thermal residual stresses within the composite which are not accounted for in this analysis (See Chapter four). It is interesting to note, however, that after the first load reversal the stress magnitudes agree. This suggests that the residual stresses in the composite dissipate rapidly. The second notable difference is the rate of hardening during plastic loading. The numerical model produced much greater hardening but this may be because it provides more rigid constraints on the unit cell than actually occur and does not incorporate any stress relaxation mechanisms.

The hysteresis loops for the T6 heat treated specimens, provided in Figure 3.10, show much less plasticity due to the limited compressive axial force which can be applied without buckling the specimen. A comparison of the hysteresis loops for the 6061-T6

aluminum alloy and composite clearly show that the composite has a lower proportional limit due to the residual stresses and stress concentrations as explained in Section 3.3.1. The T6 condition composite is stable almost immediately and does not have an appreciable hardening in the first ten cycles. The numerical results agree well with the experimental values at these low strains with a small difference in the elastic modulus.

3.3.3   Equibiaxial Cyclic Loading

In most realistic applications, it is rare to find a component which is loaded along only one axis. Multiaxial loads may be much more damaging than uniaxial loads. For example, equibiaxial loads produce shear planes which act into the body producing through thickness cracks. In a pressure vessel application similar to the test specimen, where the component experiences cyclic axial and internal pressure loads, a through thickness crack will result in loss of the pressurizing fluid. The signals the strains are forced to follow and the resulting strain path in equibiaxial loading are shown in Figure 3.11.

Figure 3.12 shows a comparison of the hysteresis loops in the axial and circumferential direction for the annealed specimen at a strain amplitude of 0.15%. Again there is good agreement between the experimental and numerical results. The only difference is greater hardening in the numerical model. Looking at the experimental results, one can see that the hoop direction shows slightly more hardening than the axial direction. This is due the specimens being made from extruded tubes. The extrusion results in grains stretched in the axial direction. Therefore, there are fewer boundaries

to dislocation movement in the axial direction. Extrusion also results in the alignment of the reinforcement.

A striking feature shown in the annealed composite is the drop in elastic modulus which occurs starting with the first load reversal when the strain amplitude is increased to 0.25% (see Figure 3.13). Within the first ten cycles, the modulus dropped by 20% and the extra loop provided shows the large drop in the modulus by loop 600. This drop in modulus under equibiaxial cyclic founding was also found to occur in this composite with only 10% reinforcement and is believed to be due to the reinforcement debonding from the matrix because of the higher effective stresses under equibiaxial loading(Ellyin, Xia, Meijer, 1993). Examples of finite element analysis with debonding are provided in (Needleman, 1987; Llorca, Needleman and Suresh, 1991). The T6 heat treated composite did not show this effect at a strain range of 0.2%, however this may be a result of the very limited amount of plasticity which occurred.

The comparison of experimental and numerical results for the T6 heat treated specimens is shown in Figure 3.14. Test strain amplitudes were limited due to buckling of the specimen therefore only a small amount of plastic deformation was achieved. One can note, however, that the areas and shape of the hysteresis loops of the test and numerical results are similar.

3.3.4   90° Out of Phase Biaxial Tests

The 90° out of phase biaxial loading shows the unique ability of the apparatus to apply complex loads. In this case the prescribed strains follow a circular path as shown

56

in Figure 3.15. This load configuration causes damage by a different mechanism than equibiaxial loading. As the strain path follows the circle, slip planes in every direction are activated driving the dislocations in different directions. This results in extra hardening. In the numerical analysis, the axial displacement was driven by the same function but was delayed by one quarter of the period of each cycle.

The experimental and numerical results for an 90° out of phase test on the annealed composite are shown in Figure 3.16. In a uniaxial or equibiaxial test, the area within the loops is proportional to the dissipated plastic strain energy or work done per cycle. However, under a 90° out of phase load the hysteresis loops may loop much different. Under elastic loading, both the axial and hoop stress-strain loops have a finite area but are generated in opposite directions. The algebraic sum of the areas is zero and the cyclic plastic strain energy is zero. When the strain amplitude is increased to the point where irreversible plastic deformation occurs one hysteresis loop will become narrower as the other grows wider. While the loops are still generated in opposite directions, there is now a net area equal to the plastic strain energy (see Xia and Ellyin, 1991). If one continues to increase the strain amplitude, the narrow loop will collapse to a line and then grow but becomes generated in the same direction as the wide loop. This behaviour is displayed in Figure 3.16. It is clear that the nonproportional path and plastic strains produce anisotropic results. Figure 3.17 shows the stresses and strains with respect to normalized time. While the strains are prescribed to be 90° out of phase the resulting stress signals are not.

Figure 3.18 shows the axial and hoop stress-strain behaviour of the composite in

the T6 condition under 90° out of phase cyclic loading. For the axial stress-strain hysteresis loop, under elastic loading, there is very good agreement between the experimental and numerical results. The loop shape and orientation are identical. The variation of stress and strain with time is shown in Figure 3.19. While the prescribed strains were 90° apart, the difference in phase angle of the stresses is only 54°. This angle is inversely proportional to the Poisson's ratio of the material and compares well with the value of 55° found from the finite element analysis. Figure 3.20 shows the strain path followed during the test and clearly shows that the maximum hoop strain during the experiment was not as high as prescribed.

The results provided in Section 3.3 show that the simple unit cell with a spherical inclusion and the Ellyin and Xia constitutive relation to model the matrix behaviour produce remarkably accurate results. Not only was this numerical method verified for cyclic uniaxial load but also equibiaxial and 90° out of phase biaxial cyclic loads. There is some difference between the numerical and experimental results for monotonic loading due to the presence of residual thermal stresses, however it was shown in Section 3.3.2 that the residual stresses dissipate quickly.
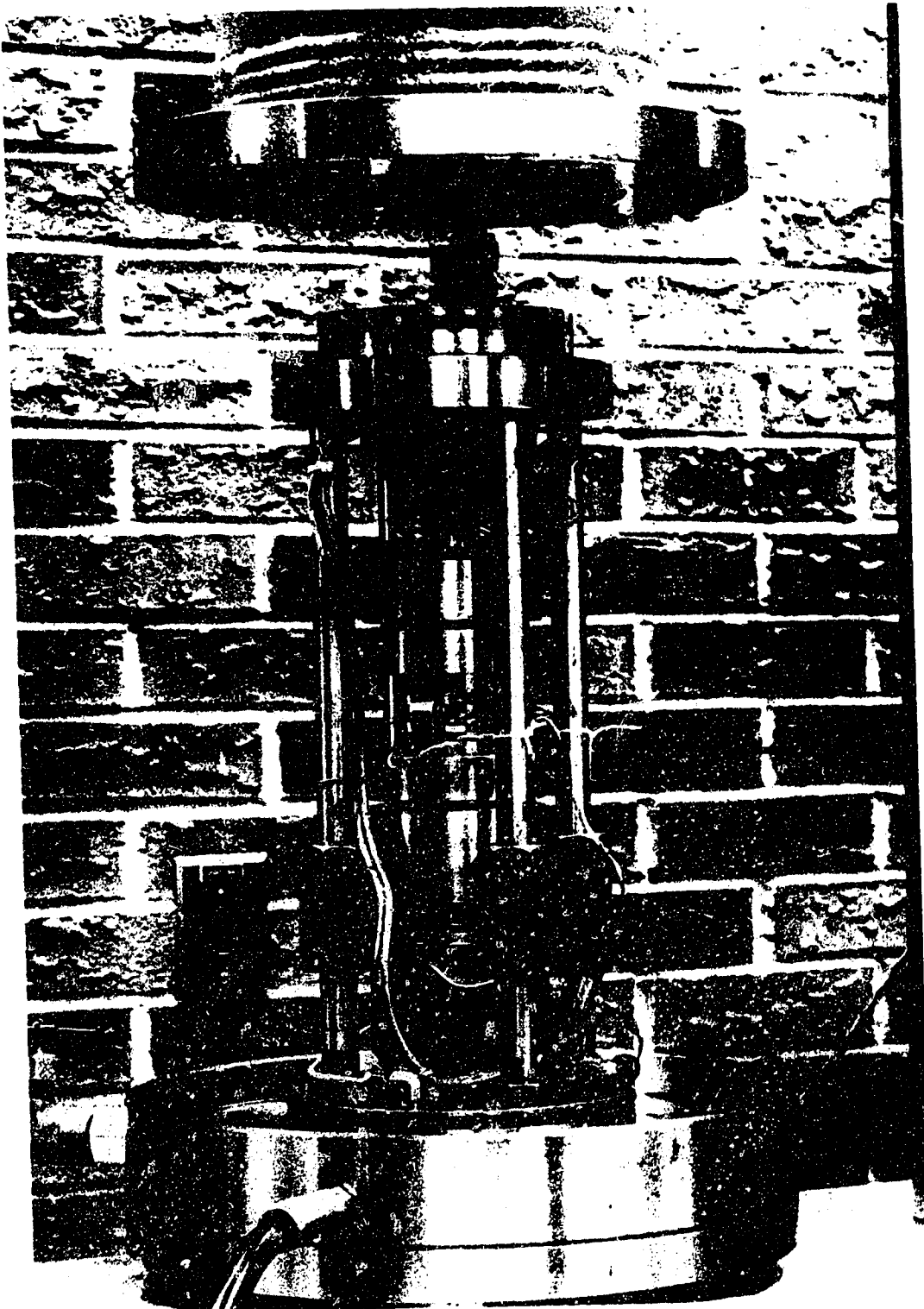
Figure 3.1: The multiaxial material testing apparatus.

59
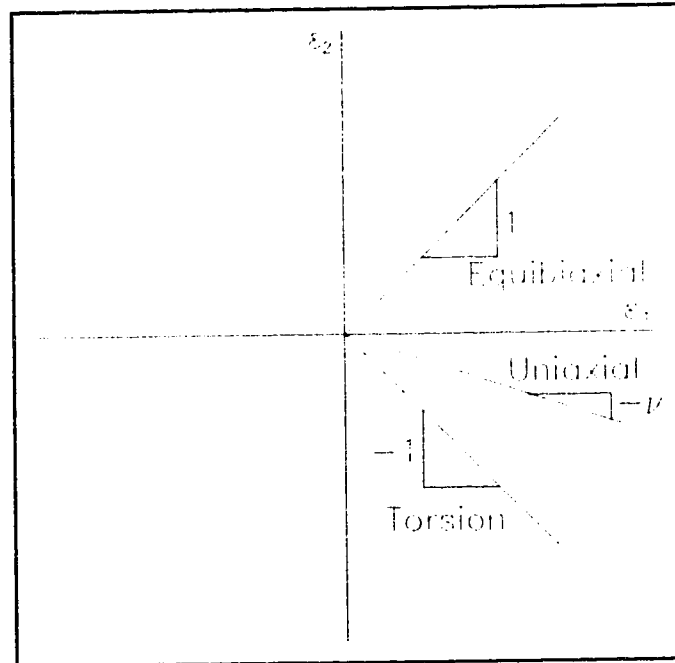
Figure 3.2: Strains paths of conventional apparatus are limited to the range between uniaxial and torsion loading. The present multiaxial testing facility allows for a strain ratio anywhere on the ϵ_1-ϵ_2 plane.

Section A—A
Dimensions in Millimetres
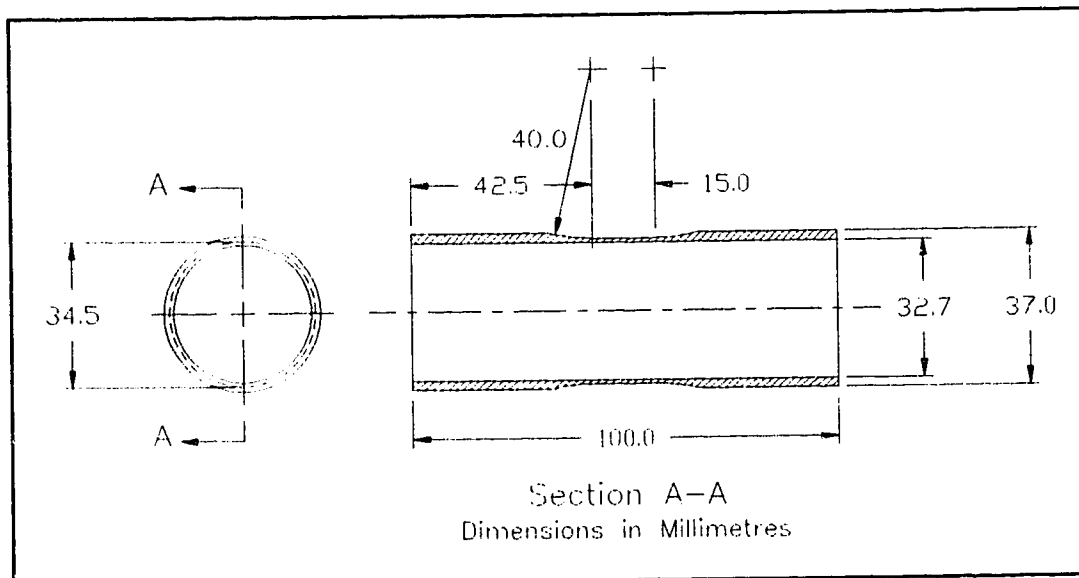
Figure 3.3: Specimen geometry for multiaxial tests.

60
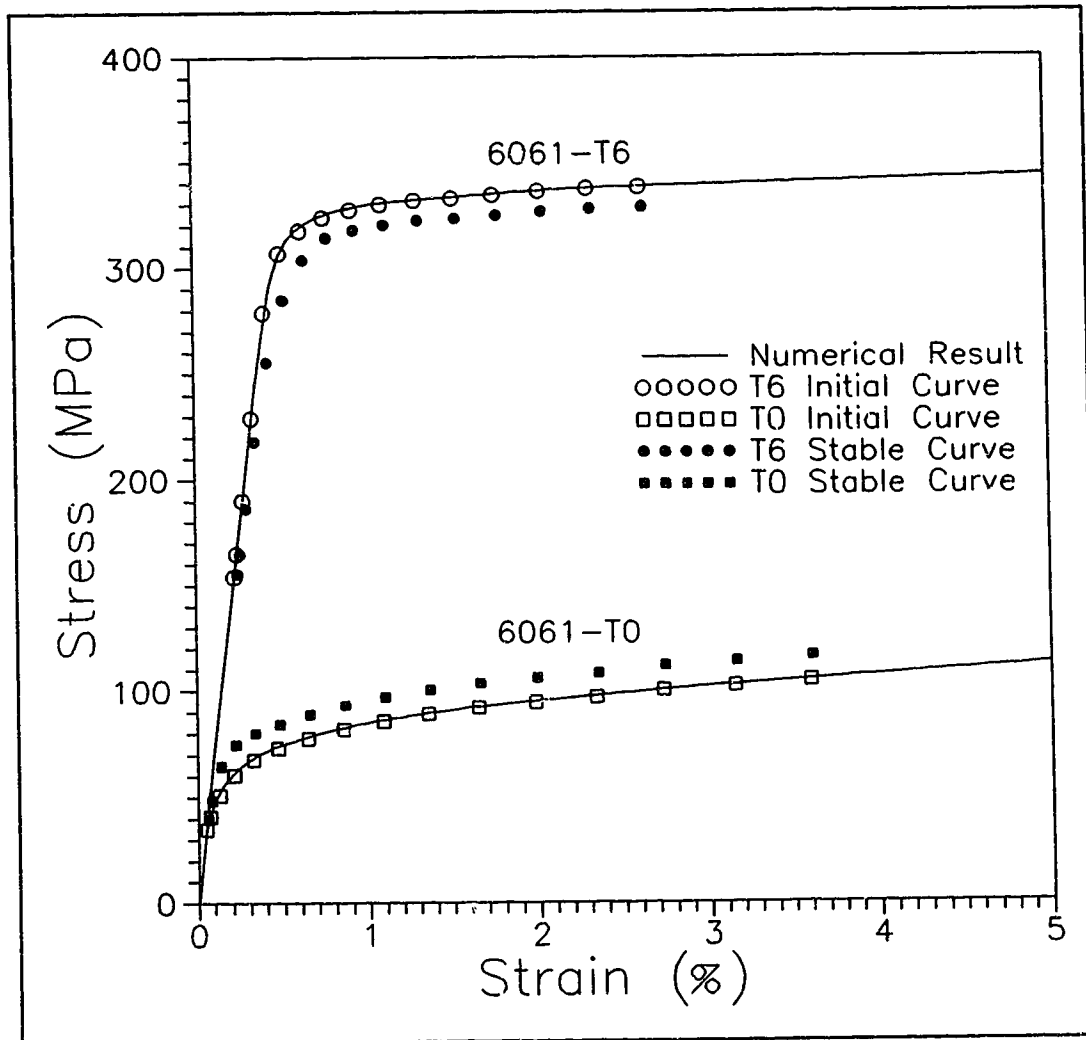
Figure 3.4: Interpolation points for the initial and stable stress-strain relations and numerical monotonic load results for 6061-T0 and 6061-T6.
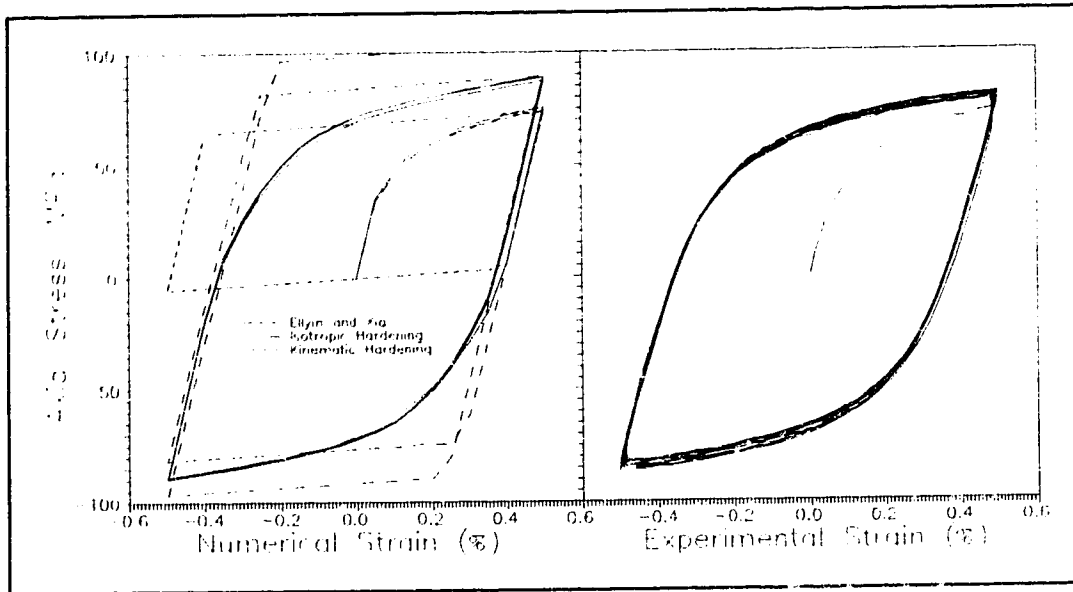
Figure 3.5: A comparison of the numerical and experimental results from the uniaxial cyclic test on 6061-T0 matrix material.
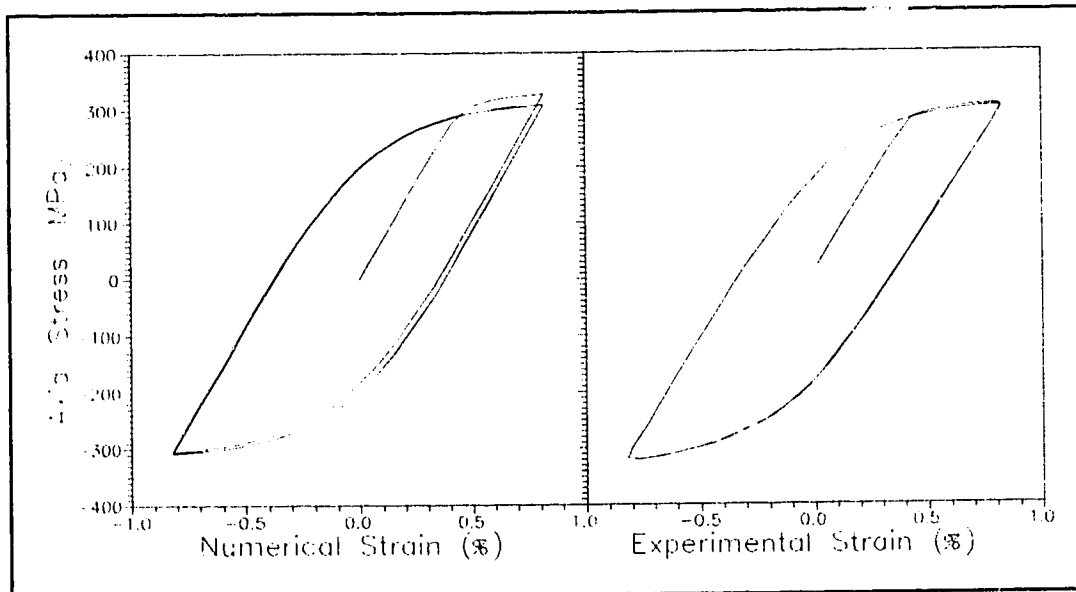
Figure 3.6: Comparison of results from the uniaxial cyclic load on 6061-T6 matrix material alone.
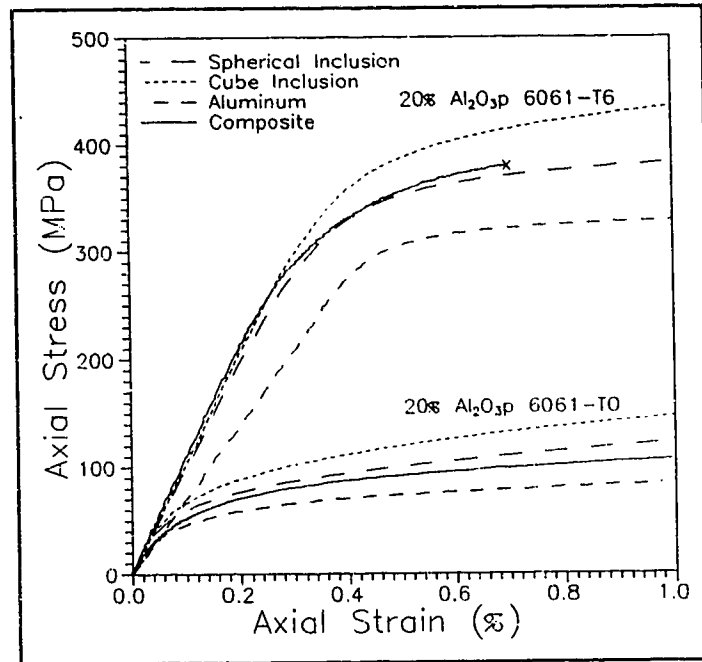
Figure 3.7: Numerical and experimental results from uniaxial monotonic loads on composite and aluminum specimens.
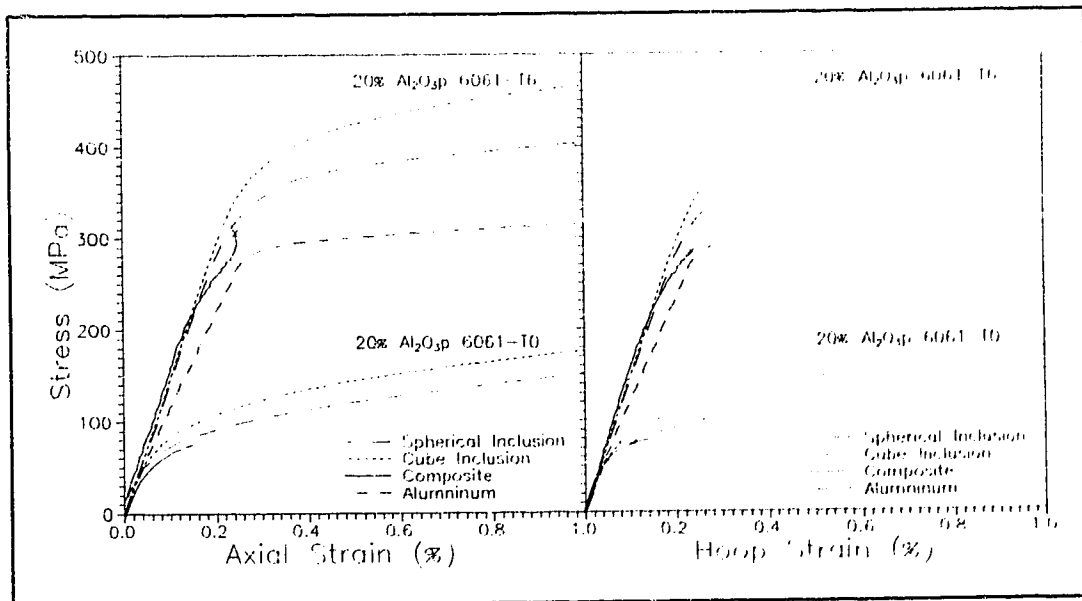
Figure 3.8: Comparison of experimental and numerical results for equibiaxial monotonic load.
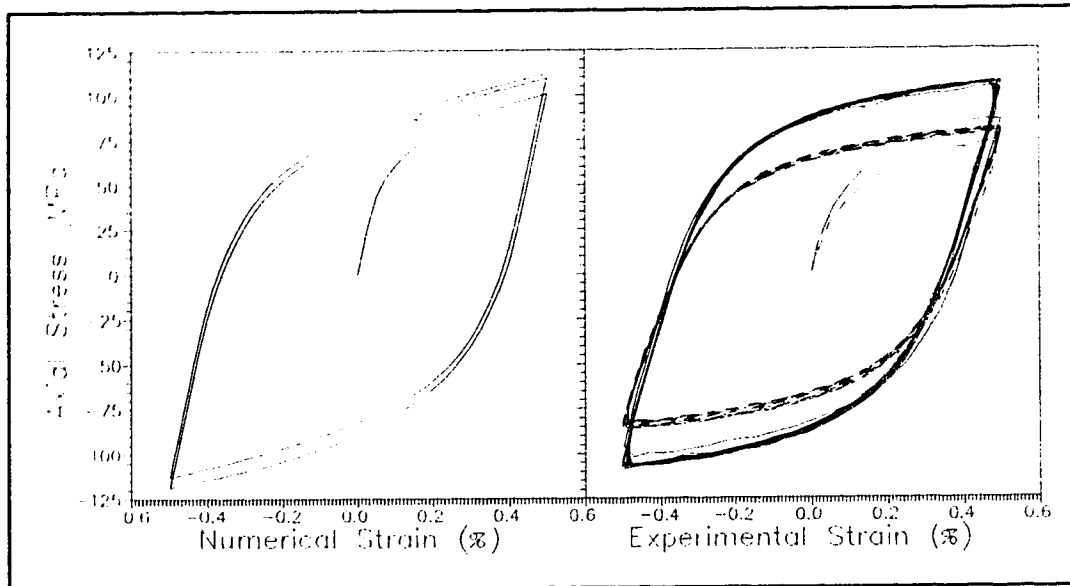
Figure 3.9: Numerical and Experimental results for uniaxial cyclic load on 20% Al_2O_3 6061-T0. Dashed line is result from 6061-T0.
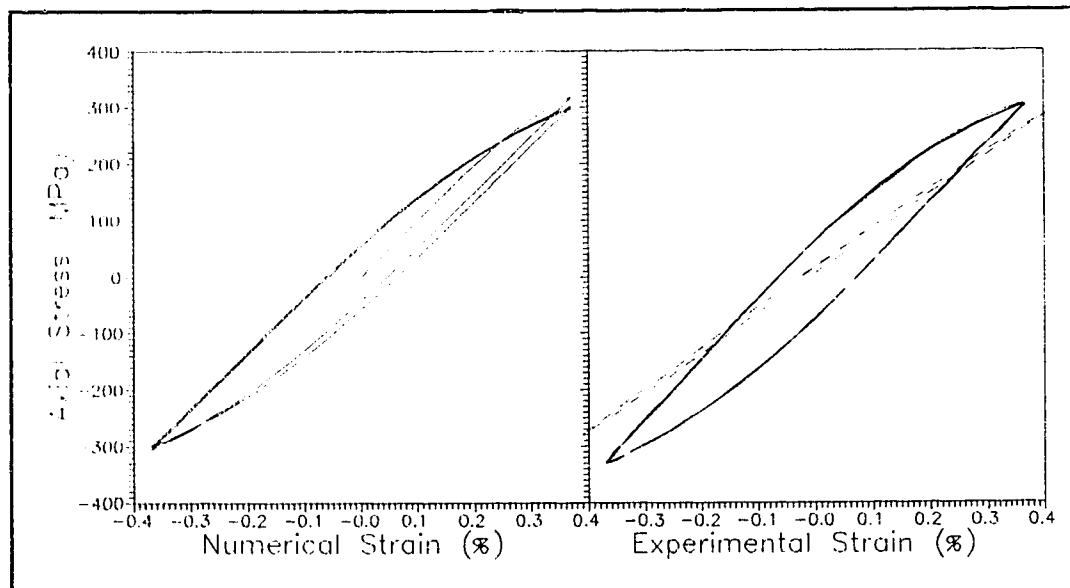
Figure 3.10: Numerical and experimental results for uniaxial cyclic load on 20% Al_2O_3p 6061-T6. Dashed line is result for 6061-T6.
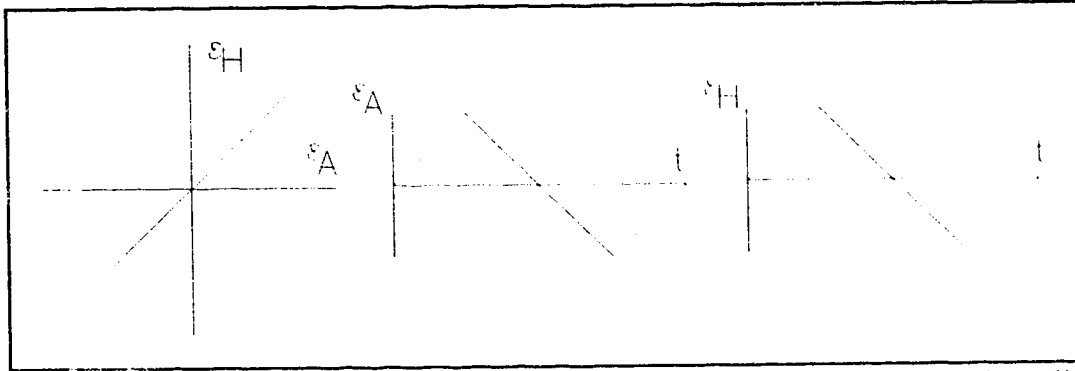
Figure 3.11: Strain path and command signals used for the equibiaxial cyclic loading.
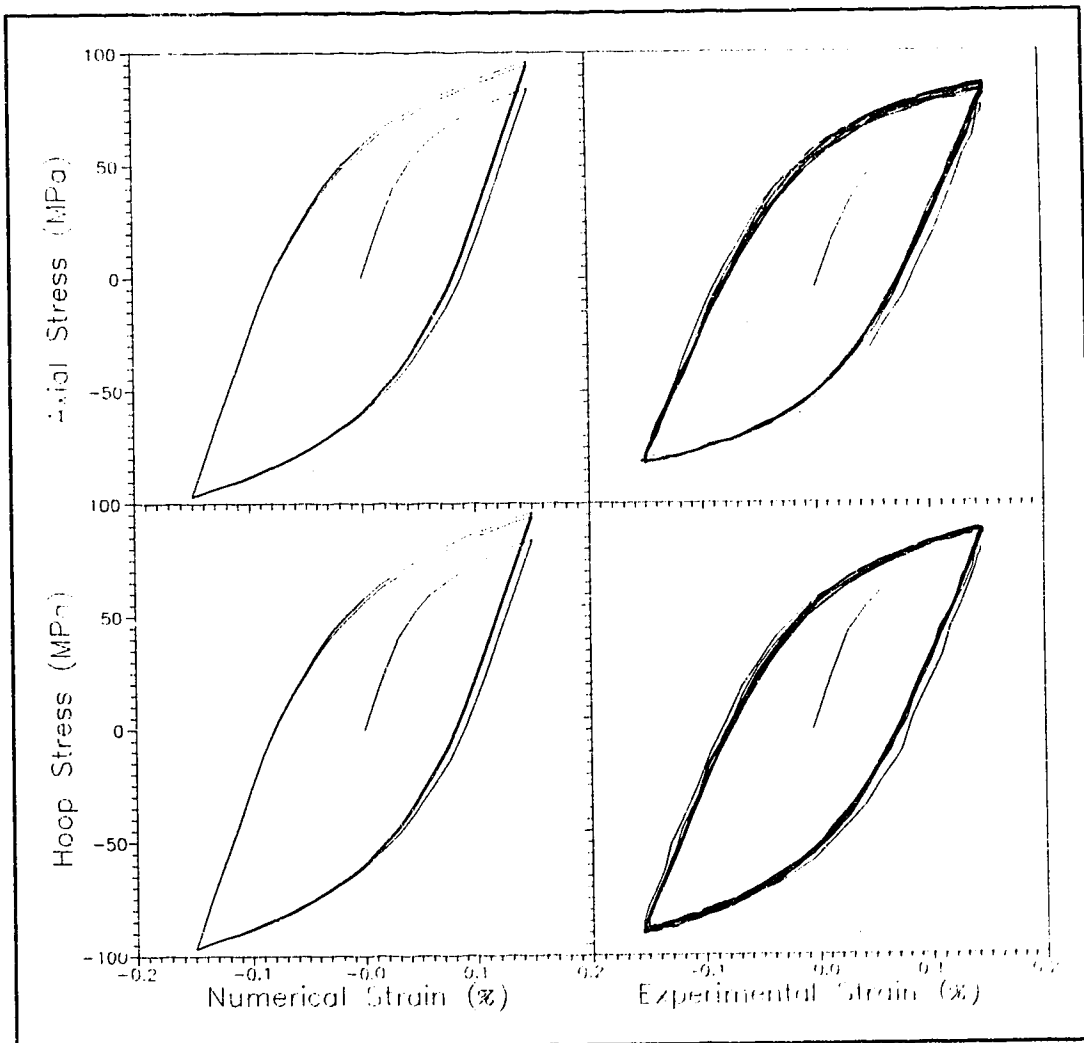
Figure 3.12: Comparison of axial and hoop hysteresis loops from the numerical and experimental analysis of an equibiaxial cyclic load on 20% Al_2O_3p 6061-T0.
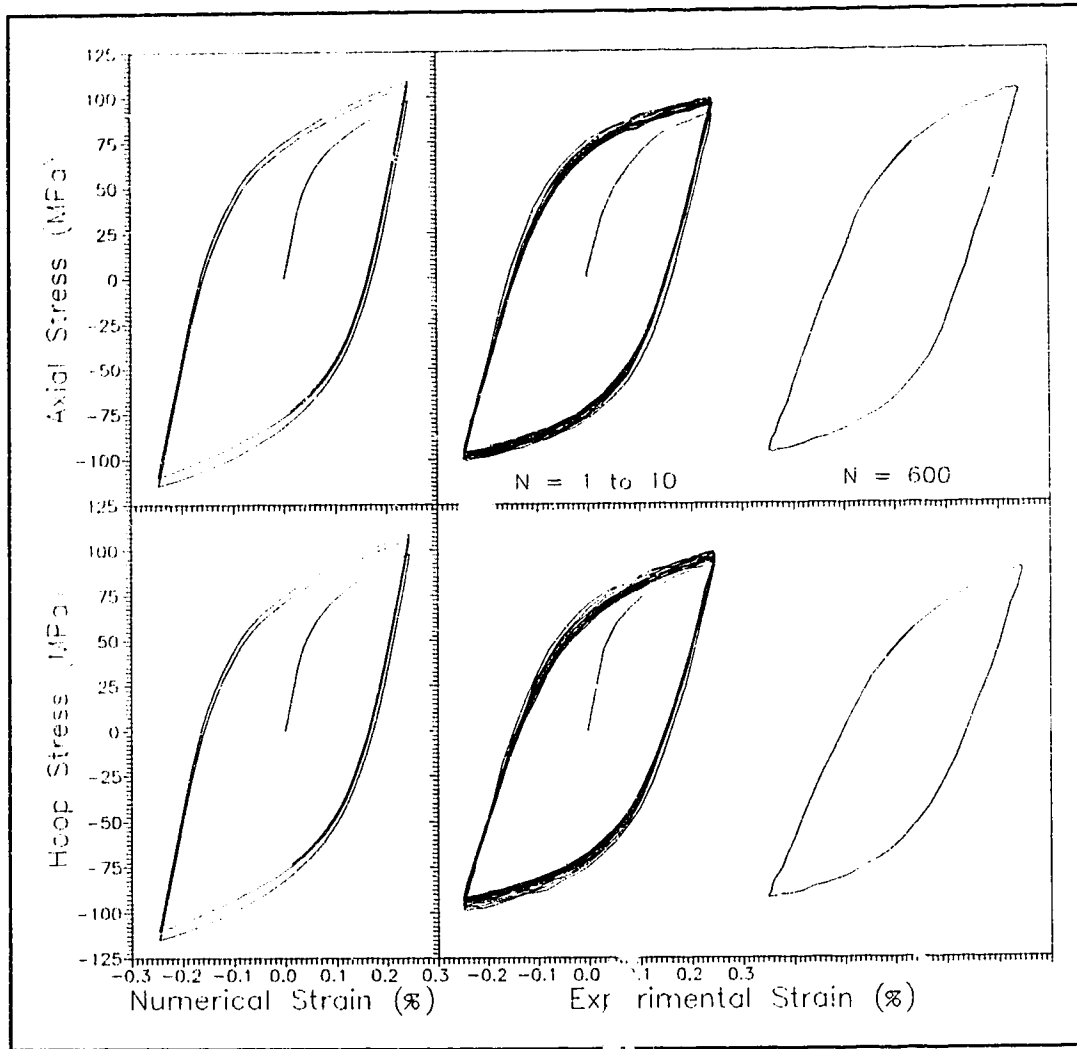
Figure 3.13: Comparison of numerical and experimental results from the 0.25% strain amplitude equibiaxial load on 20% Al₂G 6061-T0.
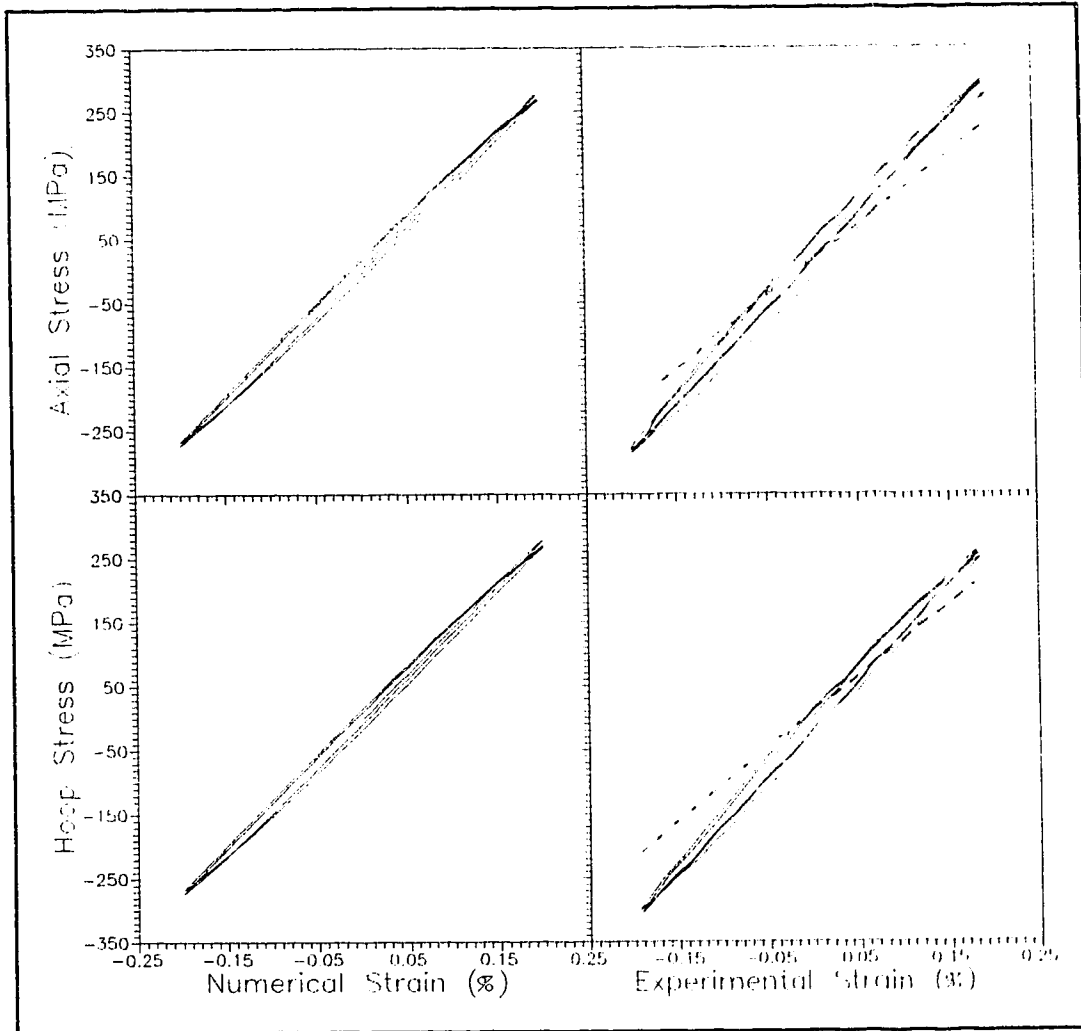
Figure 3.14: Hysteresis loops from the equibiaxial cyclic load on 20% Al_2O_3p 6061-T6. Dashed lines are results for 6061-T6.

67
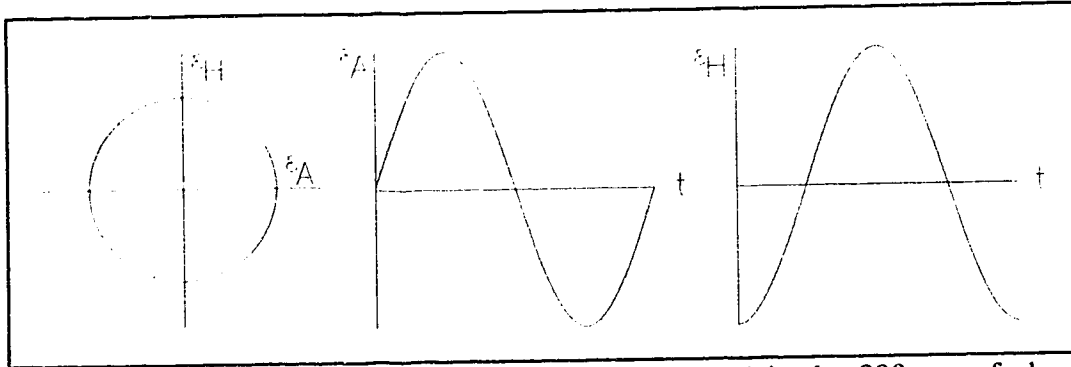
Figure 3.15: Strain path and command signals followed in the 90° out of phase biaxial cyclic test.
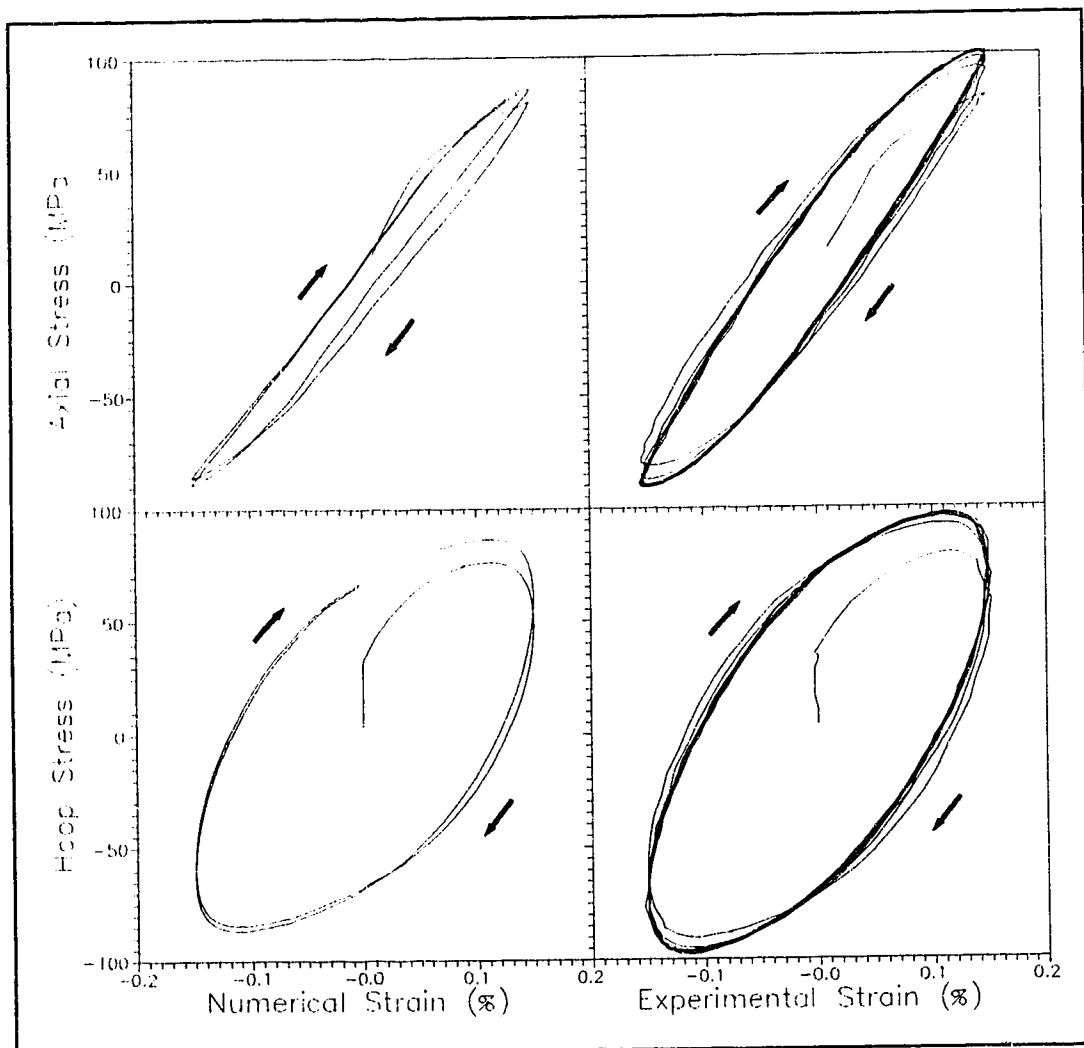
Figure 3.16: A comparison of numerical and experimental results from the 90° out of phase biaxial tests on 20% Al$_2$O$_3$p 6061-T0.
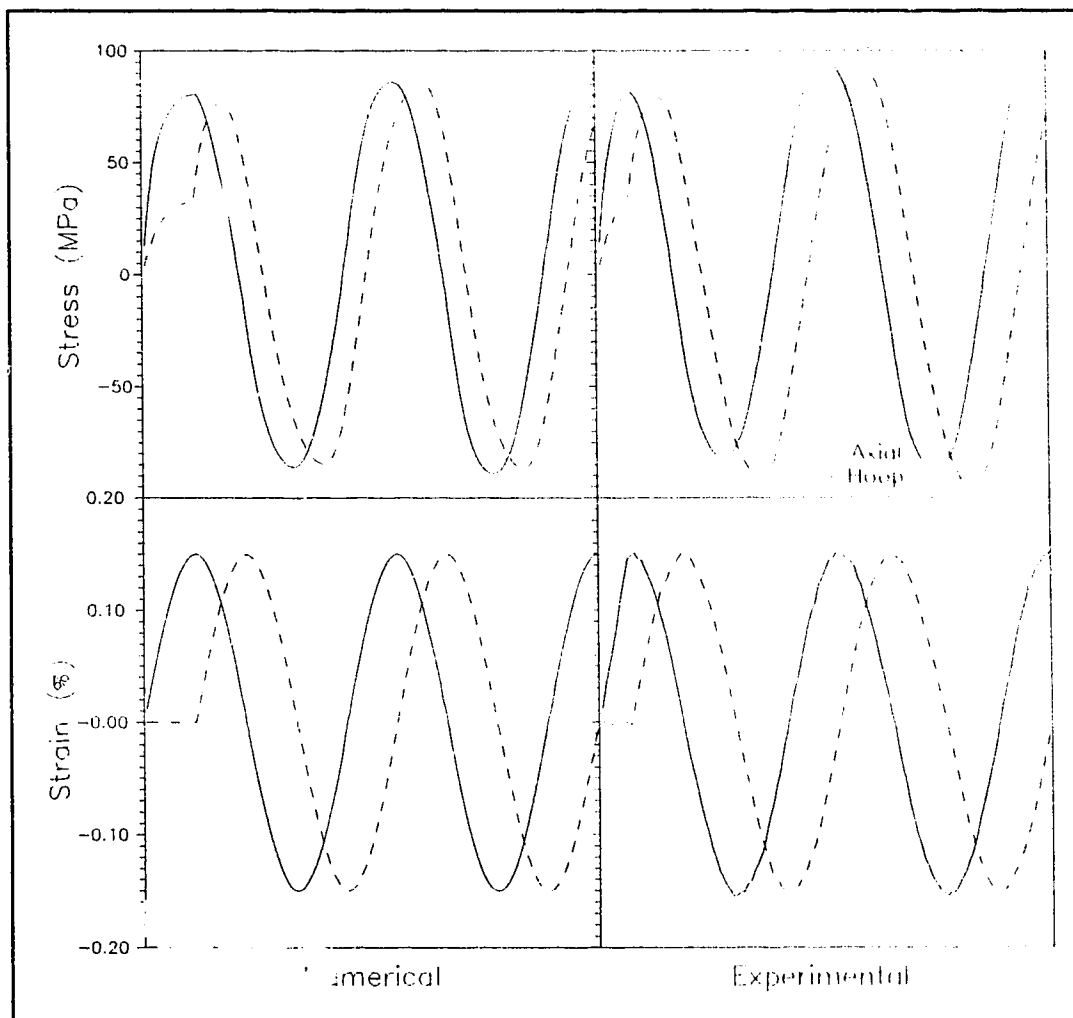
Figure 3.1? ... ution of stress and strain with respect to normalized time from the 90° out of phase biaxial cyclic test on 20% Al₂O₃p 6061-T0.
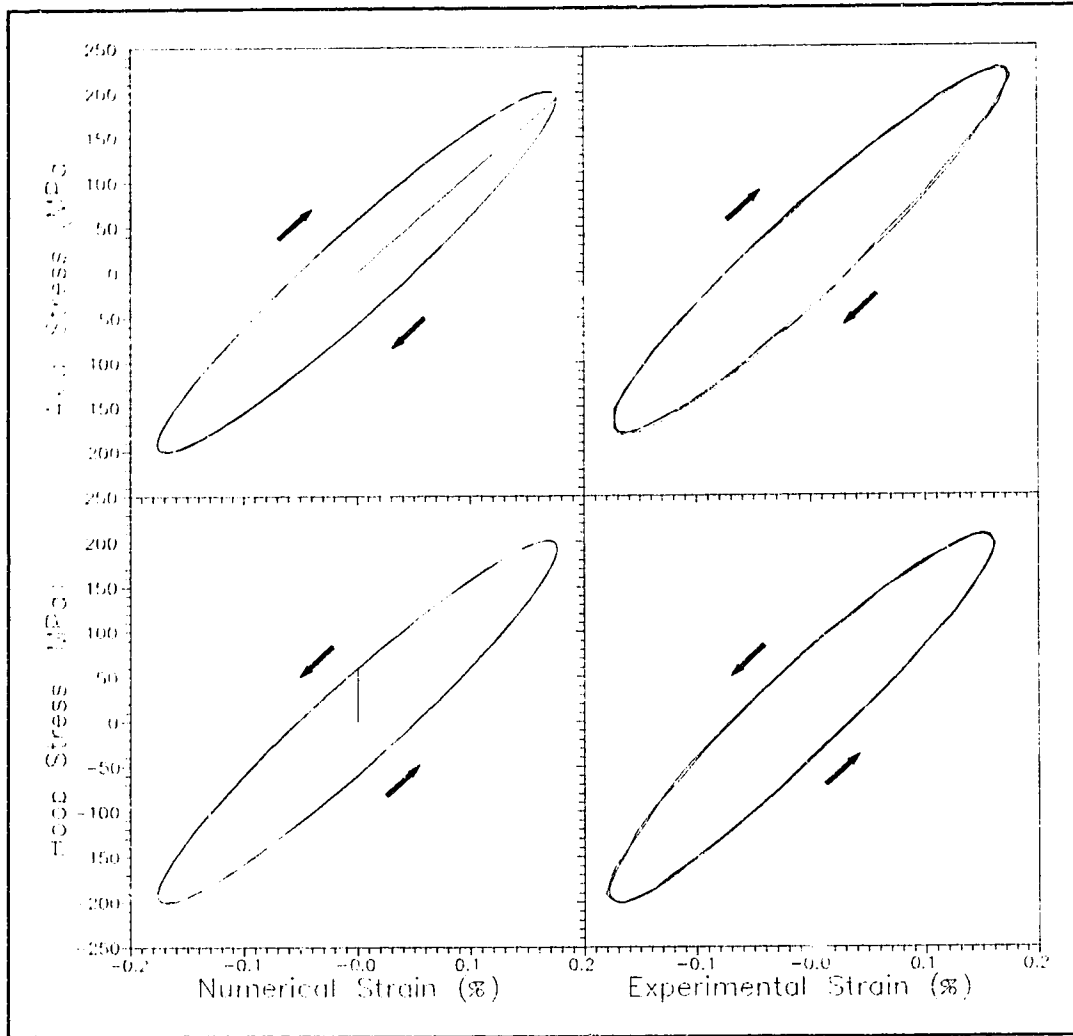
Figure 3.18: Hysteresis loops from the numerical and experimental analysis from the 90° out of phase cyclic test on 20% Al₂O₃p 6061-T6.
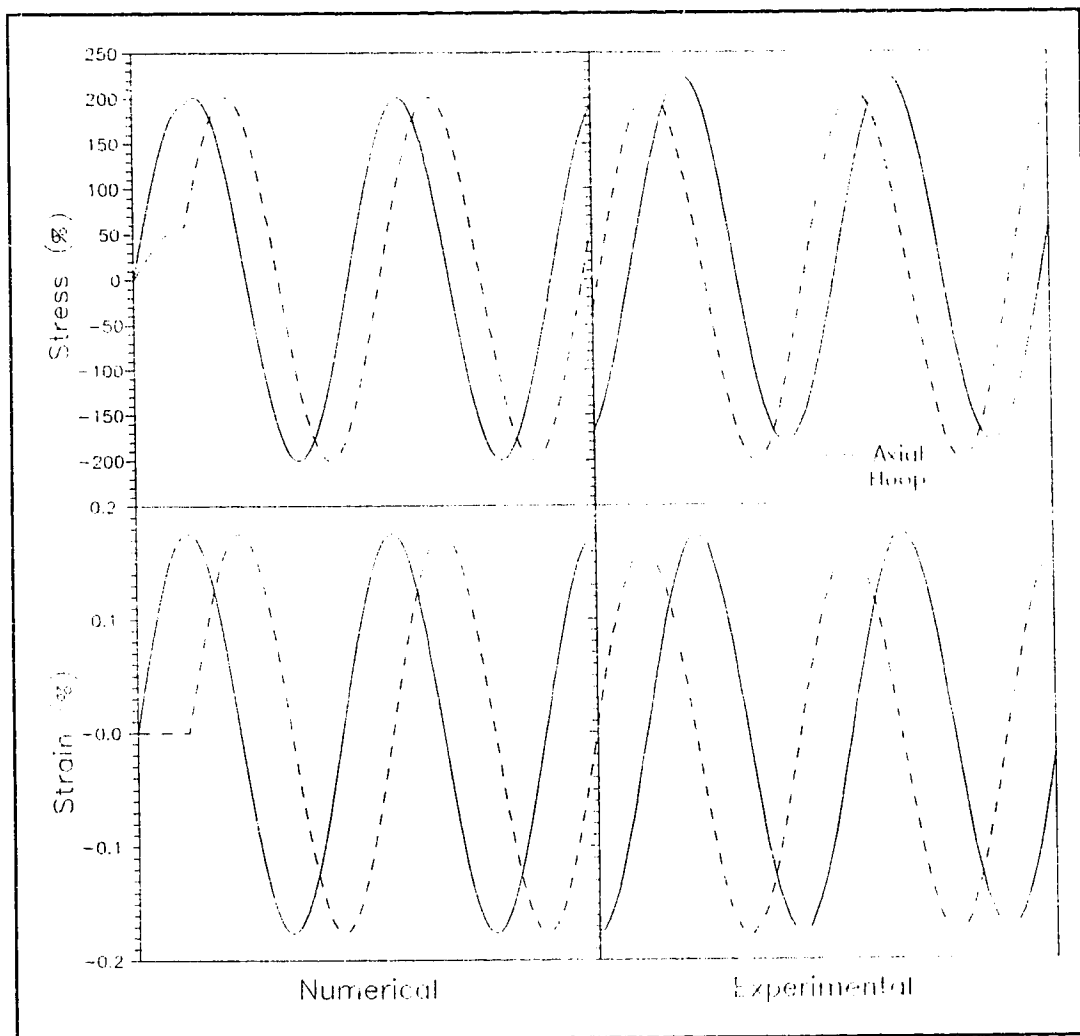
Figure 3.19: Stress and strain distribution with respect to normalized time from the 90° out of phase biaxial test on 20% Al_2O_3p 6061-T6.
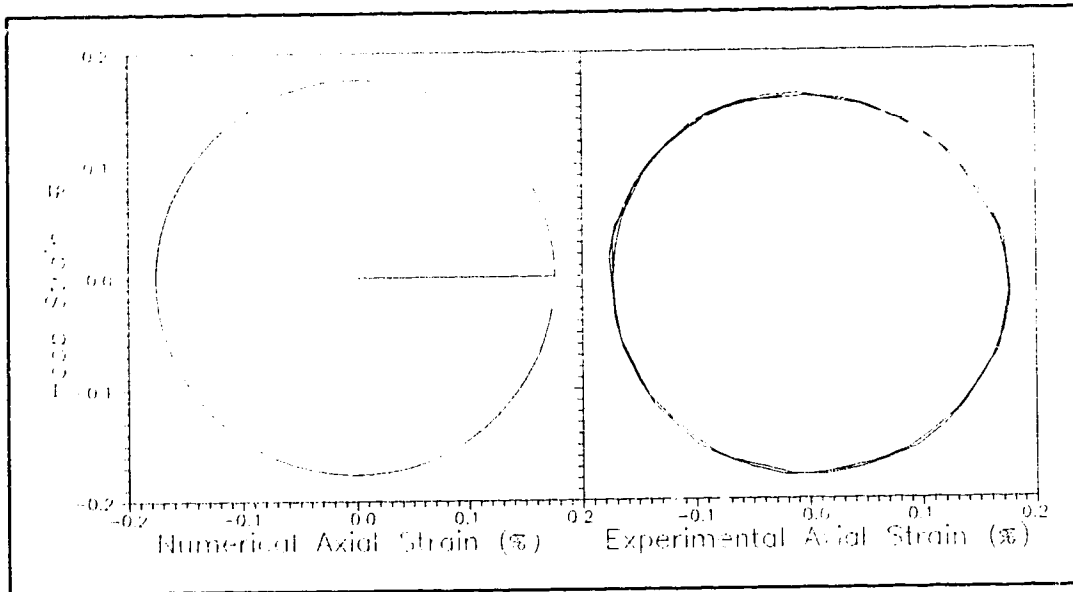
Figure 3.20: Strain paths followed for the 90° out of phase biaxial test on 20% Al₂O₃p 6061-T6.

4 Analysis of Residual Thermal Stresses

The finite element analysis results, shown in the previous chapter, were found assuming that matrix properties are the same as the aluminum alloy on its own and that the material has not experienced any previous loads or processes. One must consider, however, that these composites are generally made at high temperatures and are often subjected to further heat treatment. This will often result in residual stresses in homogeneous materials, but in particle reinforced metal matrix composites which contain large amounts of two materials, with significantly different coefficients of thermal expansion, the effects are much greater. Cooling the composite from fabrication to room temperature will then result in large residual stresses and plastic deformations in the matrix which will affect the stress-strain behaviour of the composite. Finite element analysis is useful for finding the residual stress distribution and predicting its effect on the stress-strain curve.

4.1 The Finite Element Method

The analysis of thermal residual stresses was completed using the ANSYS commercial finite element package. This software allows one to easily apply a change in body temperature and then apply an external load. Loads considered for each case, T0 and T6 heat treatment for sphere and cube inclusions were: tensile loading without a temperature drop, 480 °C temperature drop followed by tensile loading and 480 °C temperature drop followed by a compressive load. Corrections were made to compensate for the reduction in the size of the unit cell due to the temperature drop. Since the

materials have different coefficients of expansion, the volume fraction of reinforcement after the temperature drop was slightly greater, but the change was well below one percent. The kinematic hardening material model, as described in Chapter two, was used to simulate the matrix and the reinforcement was assumed to be elastic. The stress-strain data used for the kinematic hardening models consisted of five points taken from the initial curves shown previously in Figure 3.4. All of the material properties, except for the coefficient of expansion of the matrix, were treated as temperature independent and values found at 20 °C were used. The use of a room temperature yield point at all temperatures will result in higher residual stresses and smaller plastic deformations than actually occur since the yield strength of aluminum is very low at high temperatures. Boundary conditions used were as described previously and tensile and compressive uniaxial and biaxial loads were applied via external surface pressures.

4.2   Residual Thermal Stress Analysis Results

The influence of the residual thermal stresses on the composite behaviour is also dependent on factors such as the geometry of the unit cell. Therefore, the effect of particle shape on the residual stress and strain will be discussed first. This will be followed by an analysis of the stress and strain distributions after an applied load and the resulting stress-strain behaviour.

4.2.1 Influence of Reinforcement Shape on the Residual Stress Distribution

The difference in the shape of the monotonic stress-strain curve due to differences in reinforcement shape was shown in Chapter three. Without residual stresses, the unit cell containing a cube shaped inclusion had greater initial hardening and thus a much greater yield strength than that containing a spherical reinforcement. Figure 4.1 shows the equivalent stress distributions, $\sigma_e = 3/2(s_{ij}s_{ij})^{1/2}$, in unit cells containing sphere and cube shaped inclusions after a 480°C temperature drop. Figure 4.2 shows the corresponding ϵ^p_e, which is equal to I_p defined in Eq. (2.40), for each unit cell. In both cases, spherical and cube inclusion, the entire reinforcement is in compression due to the fact that the coefficient of thermal expansion of the reinforcement is $8 \times 10^{-6}/°C$ as compared to $24 \times 10^{-6}/°C$ for the 6061 aluminum matrix. Upon cooling the matrix shrinks tight around the particle resulting in compressive radial stresses and tensile circumferential stresses in the matrix around the particle. It is clear that the maximum values for stress and strain within the unit cell containing the cube are much higher, the point of highest stress and strain being at the corner tip of the inclusion. Although the values are much larger, the zone of large stresses and strains is much smaller than that in the unit cell containing the spherical inclusion. There are very small zones of large deformation undergoing strain hardening while constrained by the elastic matrix surrounding it. In the case of the spherical reinforcement, the values of stress and strain are much lower but there is still plastic deformation over a large region of the matrix around the particle. Less strain hardening is occurring and there is less constraint so load transfer from the matrix to the particle is less efficient. This results in the lower initial

hardening in the unit cell containing spherical reinforcement. Figure 4.1 also shows that the stress distribution within the spherical particle is uniform as determined by the Eshelby method.

4.2.2 Effect of Thermal Residual Stress on Subsequent Loading

Three load cases were analyzed: tensile loading with no temperature drop and tensile and compressive loading after the temperature drop. Compressive loading on its own was not done since the finite element analysis is isotropic and will result in the same stress-strain curve as tensile loading but in the third quadrant. All load conditions were modelled on unit cells containing sphere and cube shaped particles with matrices in the T0 and T6 heat treatment conditions. Simulations were done for uniaxial and equibiaxial monotonic loading. In addition, a load reversal was completed for the unit cell containing spherical reinforcement in a T0 treated matrix. These results are shown in Figures 4.3, 4.4, 4.5 and 4.6. Figures 4.7 and 4.8 show σ_e and ϵ^p_e, respectively, for the three load cases at a strain of 0.3% and figure 4.9 shows σ_x after the temperature drop only and after tensile and compressive loads following the temperature drop. Each figure for stress and strain are shown with the same contour intervals for easier comparison. These will be used to explain the influence of residual thermal stresses on the composite at small strains, large strains and after a load reversal.

Figures 4.3 and 4.4 show that, at low strains (below 0.7%), the three load conditions produce nonlinear stress-strain curves with much different initial slopes and hardening. For each composite, the tensile load with no temperature drop produces the

greatest initial hardening followed by the temperature drop and tensile load and then the temperature drop and compressive load. In fact, the results including the residual thermal stresses display nonlinear behaviour as soon as the load is applied.

This is not a drop in elastic modulus as some may suggest (Ho and Saigal, 1994) but is due to large regions of plasticity in the matrix (see figure 4.2), from the high residual stresses, before any external load is applied. Upon application of an external load, large portions of the matrix which are already plastic, expand and other regions begin to experience plastic deformation.

The difference in initial slopes agrees with the results of Zahl and McMeeking (1991) who did a similar analysis with axisymmetric models of SiC sphere and cylinder shaped particulate in an aluminum alloy matrix. They show that the initial hardening may be a function of the volume fraction of reinforcement. Jain MacEwen and Wu (1994) did similar studies on unit cells with aspect ratios greater than one. Their studies show that, in the case of short fibres, the composite is stronger in compression after a $200^{\circ}C$ temperature drop than tensile loading and this is verified by Levy and Papazian (1991). This is due to large zones of tensile residual stress around the sides of the long reinforcement.

Figure 4.7 shows that when there is no temperature drop, the stresses within the unit cell are up to 220 MPa with the highest stress in the inclusion. Tension after the quench produces an even higher stress in the inclusion. The stresses due to compression after the temperature drop are approximately one third in magnitude. In all cases, the highest stress is in the particle. It can be seen from Figure 4.8 that the particle does not

plastically deform. It is interesting to note that while the differences in stress between applying tension and compression after the quench are large, the difference between the equivalent plastic strains is 28%. The distributions of strain in these two cases look similar whereas the ϵ^p_c distribution after the tensile load only is low and quite uniform. One can suggest that in this case the greater strength is due to a greater range of elastic deformations. The reasons for difference between the tensile and compressive loading after the temperature drop are less obvious. Both unit cells contain plastic zones of similar size after the same external deformation. Under tensile loading, the magnitude of the plastic strain is much greater but the global stress-strain response shows a higher offset yield strength. Figure 4.9 shows σ_x after the temperature drop only and temperature drop followed by strain loads of 0.3% and -0.3%. From the figure, one can see that there are large compressive stresses (σ_x) between the particle and the surface on which the load will be applied after the temperature drop. Along the other side of the particle the matrix is in tension. When the temperature drop is followed by a tensile load, the stresses within the region of compression reverse and become tensile while the tensile zones experience large plastic strains. Under an applied compressive load the zones which were in tension are reversed and the zones of compression undergo plastic deformations. It is the difference in the magnitudes of the tensile and compressive residual stresses around the particle which lead to the anisotropic behaviour of the composite. The applied tensile load required to reverse the stress, from compressive to tensile, in the zone between the particle and loaded surface is greater than the compressive load needed to reverse the stress, from tensile to compressive, in the region

78

beside the particle.

Zahl and McMeeking also show that the curves for the three load conditions converge at higher strains. In Figures 4.3 and 4.4, the lines converge at approximately one percent. This convergence occurs when the entire matrix is plastically deforming and the residual stresses no longer have any influence. At this point, the load transfer effects due to inclusion shape have vanished and the increase in stress is due to the strain hardening of the matrix. This is why the stress-strain curves, for the three load cases, become parallel. Figures 4.5.and 4.6 show the stress-strain response of the composite to equibiaxial loads. The effects are similar, however there is greater plasticity at small strains due to the higher effective strain, and the curves converge at a lower strain. Under the equibiaxial loading, the axial and hoop stress strains will look identical so only one direction is shown.

It was seen in Section 3.3.2 that the results of the uniaxial cyclic numerical analysis match the experimental data after the first load reversal. This effect was studied for the three loading cases on the unit cell with the spherical inclusion and annealed matrix by the loading the unit cell to 90 MPa and then dropping it to 0 MPa. Upon load reversal, all three cases have the same modulus which is identical to the initial elastic modulus for the composite without a prior temperature drop. This supports the previous conclusion that residual stresses dissipate rapidly under cyclic loading.

Clearly the residual stresses are an important factor in determining the monotonic stress-strain behaviour of these particulate reinforced composites. Results of small strain amplitude cyclic studies from Chapter three, however, show that the effects of residual stresses disappear after load reversal.
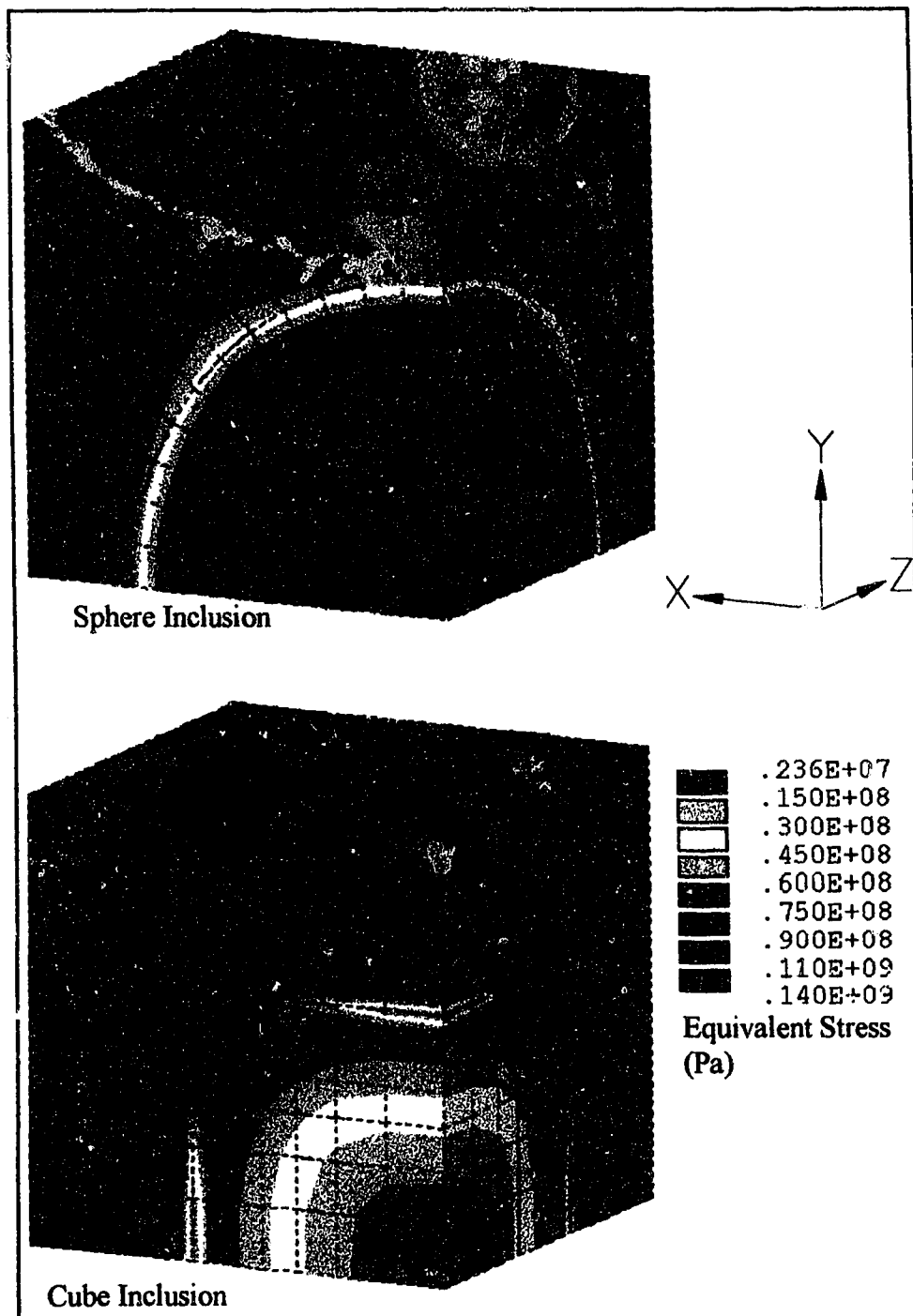
Figure 4.1: Residual equivalent stress distribution after 480 °C temperature drop in unit cells containing sphere and cube shaped reinforcement.

81
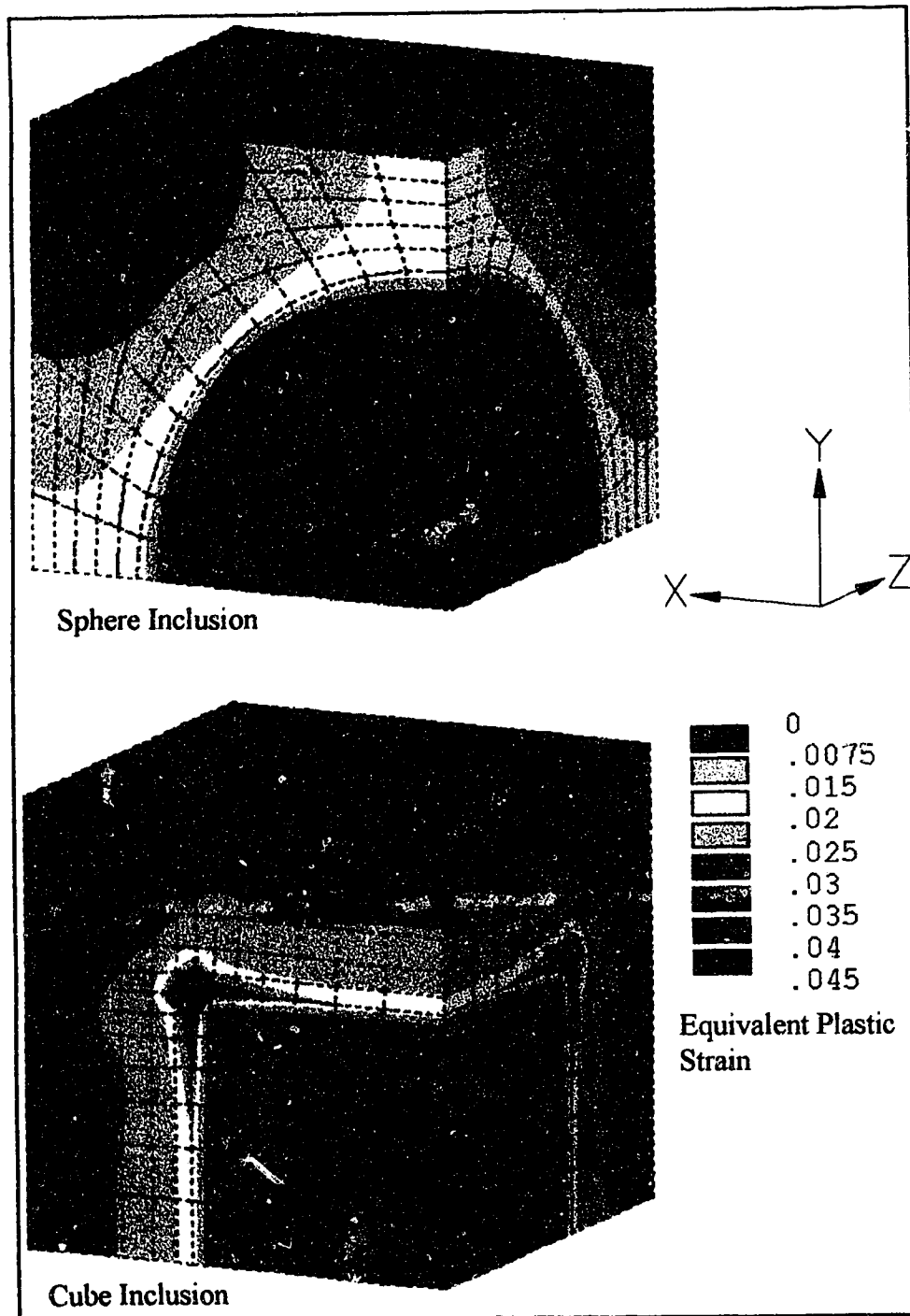
Figure 4.2: Residual equivalent plastic strain after 480 °C temperature drop in unit cells containing sphere and cube shaped particles.
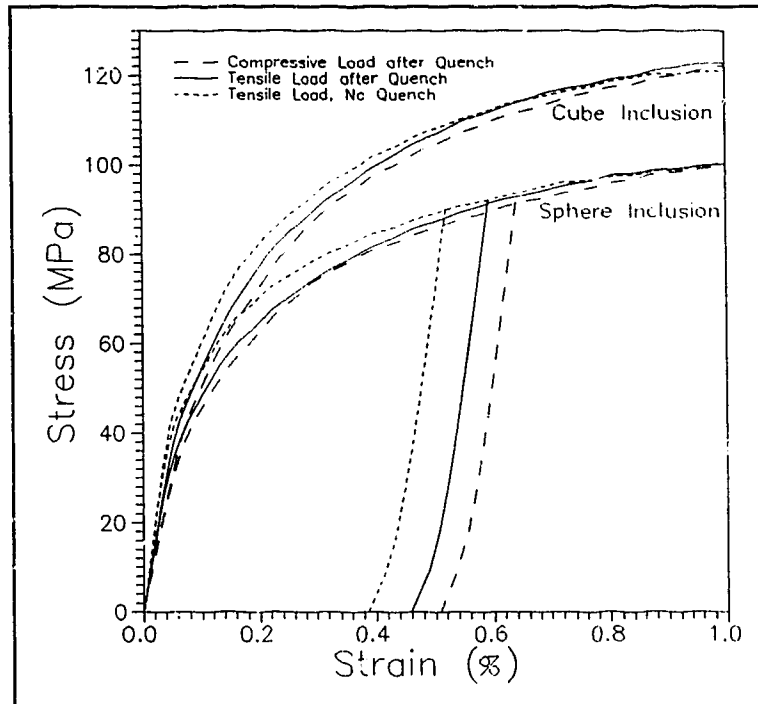
Figure 4.3: Results of thermal residual stress analysis on 20% Al_2O3_p 6061-T0.
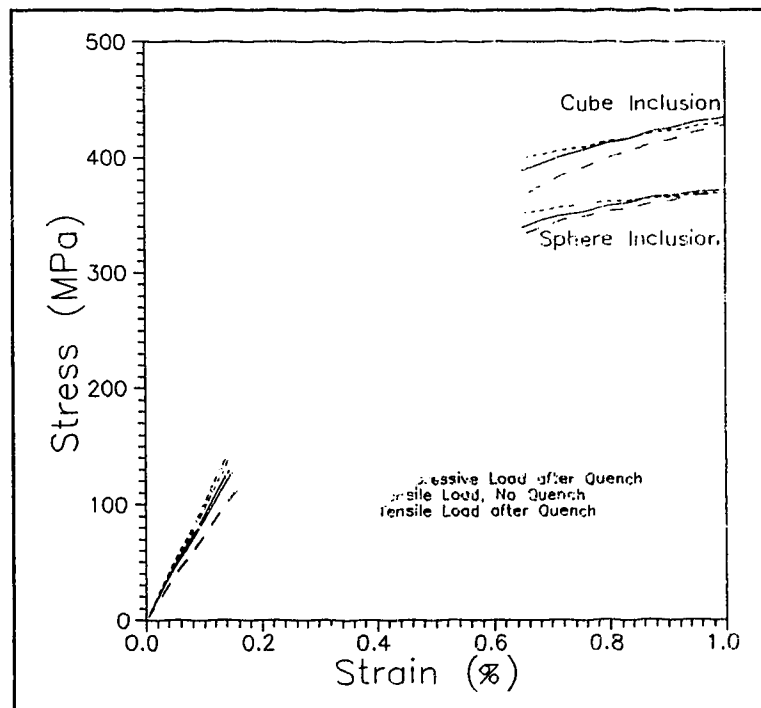
Figure 4.4: Stress-strain relations from finite element analysis on 20% Al_2O_3p 6061-T6.

83
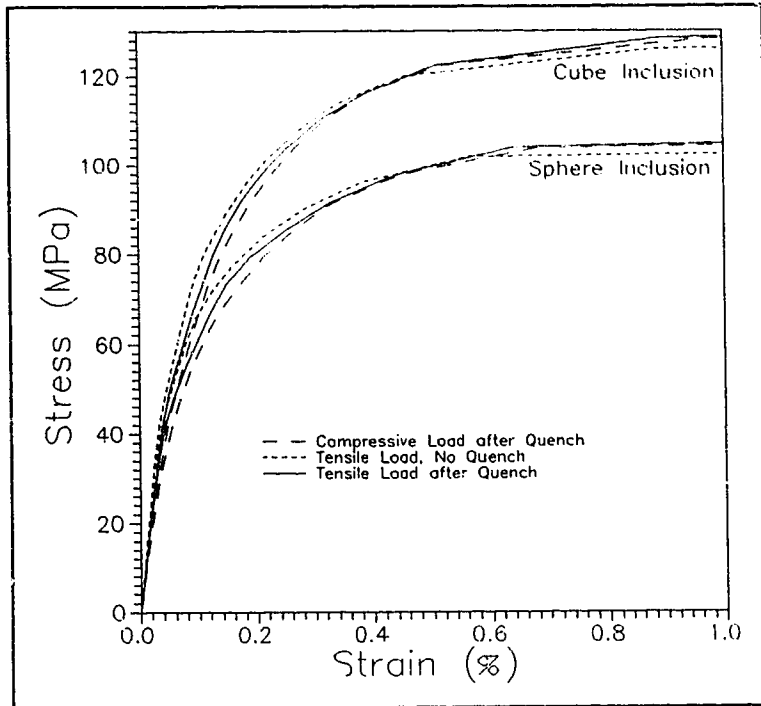
Figure 4.5: Results of the equibiaxial load in the thermal residual stress analysis of 20% Al₂O₃p 6061-T0.
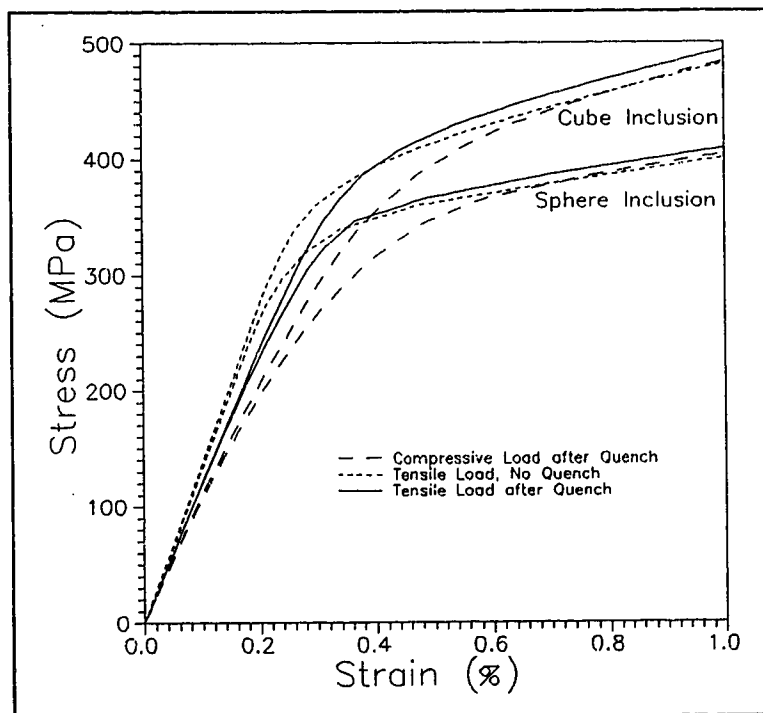
Figure 4.6: Results of the equibiaxial load on the thermal residual stress analysis on 20% Al₂O₃p 6061-T6.

84

$\Delta T = 0\ ^\circ C\ \ \varepsilon_x = 0.3\%$

$\Delta T = 480\ ^\circ C\ \ \varepsilon_x = 0.3\%$

$\Delta T = 480\ ^\circ C\ \ \varepsilon_x = -0.3\%$

```
.100E+08
.362E+08
.625E+08
.888E+08
.115E+09
.141E+09
.168E+09
.194E+09
.220E+09
```

Equivalent Stress (Pa)
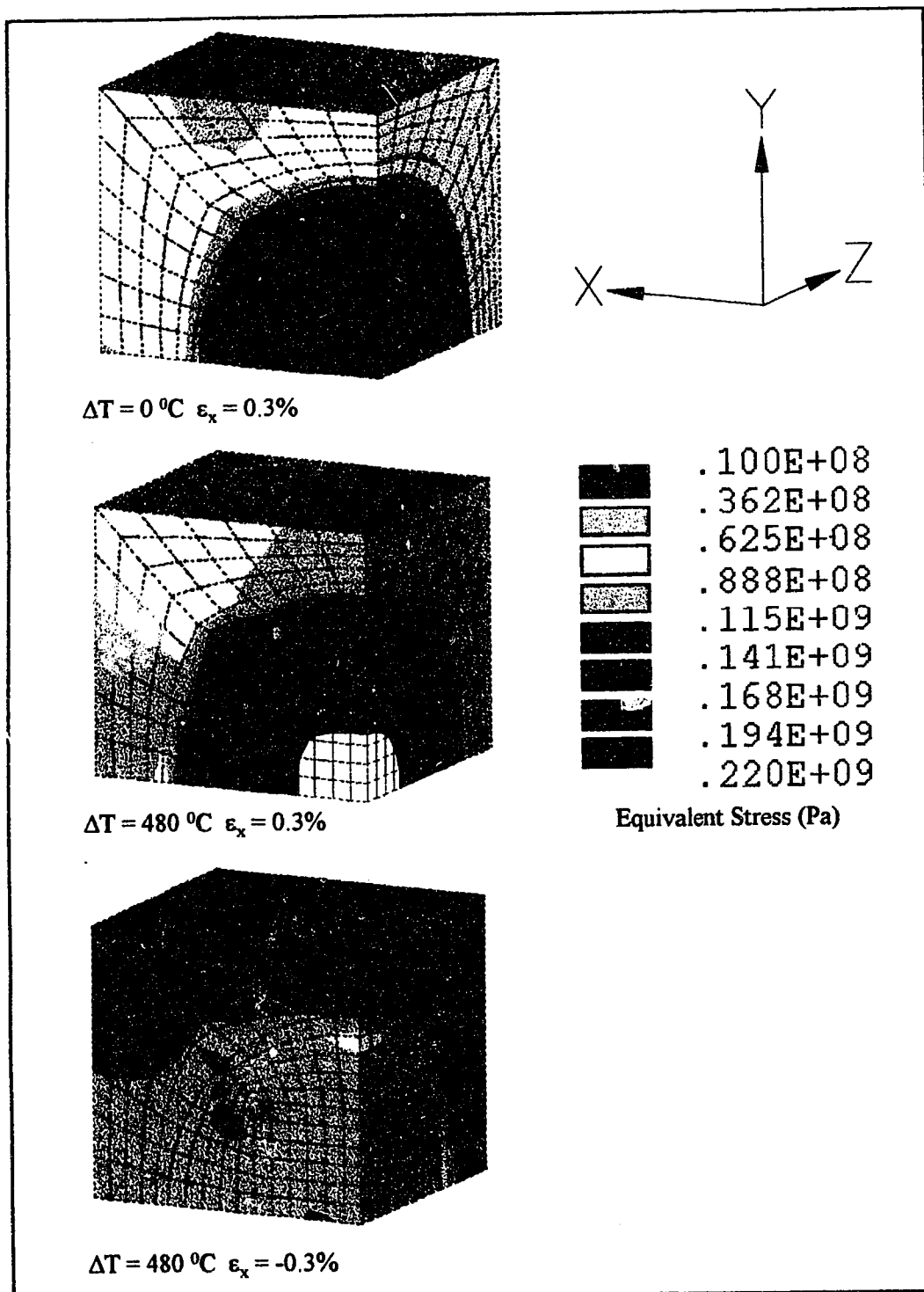
Figure 4.7: Equivalent stress distribution after three load conditions are applied to a 20% Al_2O_3 6061-T0 unit cell containing spherical reinforcement.

ΔT = 0 °C ε_x = 0.3%

ΔT = 480 °C ε_x = 0.3%

ΔT = 480 °C ε_x = -0.3%

.510E-03
.01125
.0225 ·
.03375
.045
.05625
.0675
.07875
.09

Equivalent Plastic Strain
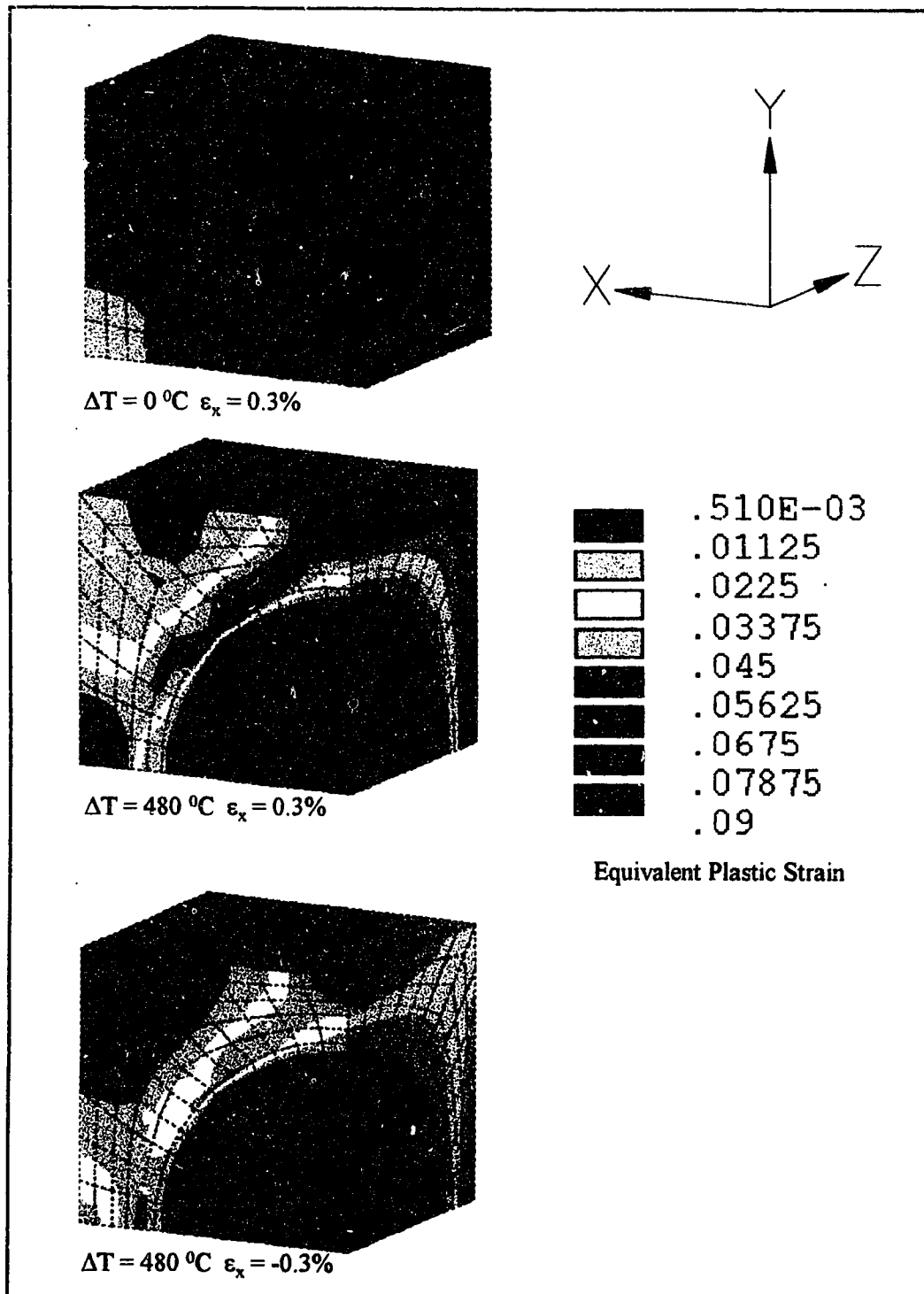
Figure 4.8: Equivalent plastic strain distribution after the three load conditions are applied to a 20% Al_2O_3 6061-T0 unit cell containing spherical reinforcement.

$\Delta T = 480\ ^oC\ \varepsilon_x = 0.0\%$

$\Delta T = 480\ ^0 C\ \varepsilon_x = 0.3\%$

$\Delta T = 480\ ^0 C\ \varepsilon_x = -0.3\%$

$-0.106E+09$
$-0.700E+08$
$-0.300E+08$
$0.100E+08$
$0.500E+08$
$0.900E+08$
$0.130E+09$
$0.170E+09$
$0.220E+09$

σ_x (Pa)
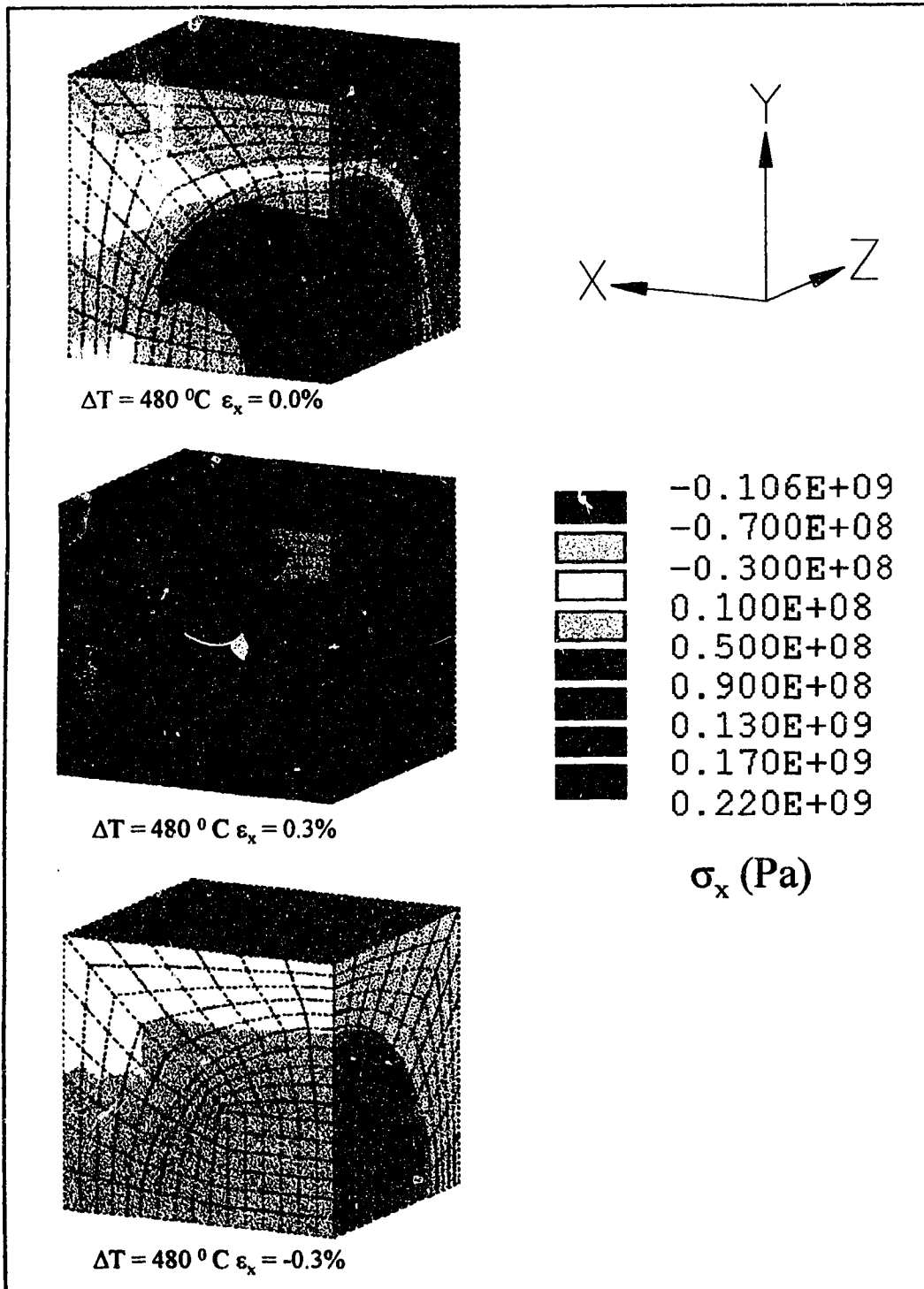
Figure 4.9: σ_x after a 480 ^oC temperature drop, temperature drop and tensile load and temperature and compressive load on a 20% Al_2O_3 6061-T0 unit cell containing spherical reinforcement.

5 Conclusions and Future Work

5.1 Conclusions

The primary goal of this study was to model the behaviour of 20% Al_2O_3p 6061 aluminum composite under complex multiaxial loads using a three-dimensional finite element analysis with a more advanced two surface constitutive relation. Considerations included the effectiveness of the material model and adequacy of the simple unit cell model and reinforcement geometry. These were tested under very complex load situations. The effects of residual stresses within the unit cell due to processing were also studied. The results presented provide some clear conclusions.

1:    The Ellyin and Xia constitutive relation, used to model the aluminum matrix, was shown to be superior to the common isotropic and kinematic hardening models. It has the capability to produce cyclic hardening as well as extra hardening due to nonproportional loading paths. Its ability to model the homogeneous matrix materials was shown for both the T0 and T6 heat treated 6061 aluminum alloy under uniaxial cyclic loads. Its superiority was also shown in the modelling of the composite materials. It clearly produces the hardening characteristics found from experiments. The Ellyin and Xia material model is much more suitable for simulating cyclic strain hardening materials than traditional constitutive relations.

2:    The fairly simple unit cell model combined with the use of the Ellyin and Xia constitutive relation to model the matrix, has been used extensively to model particulate reinforced composites. The assumption of a perfectly aligned array of identical inclusions would seem to under estimate the mechanisms acting within the composite

however, the finite element results using a spherical inclusion show very good agreement with experimental results in both qualitative and quantitative manners under multiaxial nonproportional cyclic loading, i.e: lower proportional limit, transient hardening and softening. These suggest that load transfer is the primary mechanism of strengthening in the composite.

3:    The difference between cube and sphere shaped particles was clearly shown. Cube inclusions produce much higher stress concentrations in smaller zones of the matrix leading to greater initial hardening and, therefore, higher yield stresses due to localization of plasticity. The inclusions in the composite have sharp edges and corners however, the experimental results agree closely with the numerical analysis using a spherical inclusion.

4:    Monotonic loading was found to be strongly influenced by residual stresses. The metal matrix composites are generally produced at a high temperature and then cooled. This process introduces significant thermal residual stresses and results in anisotropic behaviour. That is, the initial hardening of the composite is greater under a tensile load than a compressive load. The analysis with no thermal stresses resulted in a higher proportional limit and greater initial hardening but at large strains all three load cases resulted in similar stresses. When the matrix becomes fully plastic, the difference in the stress-strain curves is due to strain hardening of the matrix. It was shown that after the first load reversal the effects of residual stresses are negligible.

These conclusions will be useful for research to be done in the future. Both the unit cell approach and the material model have been validated under complex multiaxial loads. It is also clear that residual thermal stresses, due to processing, significantly influence the stress-strain behaviour of particulate reinforced metal matrix composites under monotonic loads.

5.2 Future Research

Recently there has been a large amount of research on the behaviour of discontinuously reinforced metal matrix composites covering many of the variables in these materials. These may include reinforcement geometry, size and distribution as well as mechanisms operating in the matrix. The use of the material model described in this thesis to simulate the matrix, will allow these studies to be done accurately for complex cyclic loads. This will produce results which are more useful for design with these materials. Although the load transfer mechanism has been shown to be dominant at low strain amplitudes, it is quite clear that damage is occurring at large accumulated strains. The reduction of the stiffness in the composite under equibiaxial loads seems to suggest debonding at the particle matrix interface and this should be studied using a progressive debonding model.

References

ANSYS User's Manual, Revision 5.0 Volume IV: Theory, Swanson Analysis Systems Inc., 1992

Arsenault, R: Strengthening of Metal Matrix Composites Due to Dislocation Generation Through CTE Mismatch, Metal Matrix Composites: Mechanisms and Properties, Academic Press Inc., 1991

Arsenault, R. and R. Everett (Eds.): Metal Matrix Composites: Processing and Interfaces, Acedemic Press Inc., 1991

Arsenault, R., and M. Taya: Thermal Residual Stress in Metal Matrix Composite, Acta Metall. Vol. 35, No. 3, pp. 651-659, 1987

Arsenault, R., L. Wang and C. Feng: Strengthening of Composites Due to Microstructural Changes in the Matrix, Acta Metall. Mater. Vol. 39, No. 1, pp. 47-57, 1991

Bao, G.: Damage Due to Fracture of Brittle Reinforcements in a Ductile Matrix, Acta Metall. Mater. Vol. 40, No. 10, pp 2547-2555, 1992

Boardman, B.: Metal Matrix Composites - "An Opportunity for Off-Highway Industry", SAE SP-836, 1990

Christman, T., A. Needleman and S. Suresh: An Experimental and Numerical Study of Deformation in Metal-Ceramic Composites, Acta Metall. Vol. 37, No. 11, pp. 3029-3050, 1989

Christman, T. and S. Suresh: Microstructural Development in an Aluminum Alloy-SiC Whisker Composite, Acta Metall. Vol. 36, No. 7, pp. 1691-1704, 1988

Clyne, T. and P. Withers: An Introduction to Metal Matrix Composites, Cambridge University Press, 1993

Corbin, S. and D. Wilkinson: The Influence of Particle Distribution on the Mechanical Response of a Particulate Metal Matrix Composite, Acta Metall. Mater. Vol. 42, No. 4, pp. 1311-1318, 1994

Ellyin, F.: An Anisotropic Hardening Rule for Elastoplastic Solids Based on Experimental Observations, Journal of Applied Mechanics Vol. 56 or 111, pp. 499-507, 1989

Ellyin, F. and J. Wu: Elastic-Plastic Analysis of a Stationary Crack Under Cyclic Loading and Effect of Overload, *International Journal of Fracture* Vol. 56, pp 189-208, 1992

Ellyin, F. and Z. Xia: A Rate-Independent Constitutive Model for Transient Non-Proportional Loading, *J. Mech. Phys. Solids* Vol. 37, No. 1, pp. 71-91, 1989

Ellyin, F., Z. Xia and G. Meijer: Effect of Multiaxial Cyclic Loading on the Damage of Particulate Reinforced Metal Matrix Composites, MECAMET 93 International Seminar on Micromechanics of Materials, pp. 418-426, 1993

Ellyin, F., Z. Xia and J. Wu: A New Elasto-Plastic Constitutive Model Inserted Into the User-Supplied Material Model of ADINA, *Computers and Structures*, 1995, To be published.

Eshelby, J.: The Determination of the Elastic Field of an Ellipsoidal Inclusion, and Related Problems, *Royal Society of London Proceedings A* Vol 241, pp. 376-396, 1957

Ho, S. and A. Saigal: Thermal Residual Stresses and Mechanical Behaviour of Cast SiC/Al Composites, *Materials Science and Engineering* Vol. A183, pp. 39-47, 1994

Hom, C.: Three-Dimensional Finite Element Analysis of Plastic Deformation in a Whisker-Reinforced Metal Matrix Composite, *J. Mech. Phys. Solids* Vol. 40, No. 5, pp. 991-1008, 1992

Jain, M., S. MacEwen and L. Wu: Finite Element Modelling of Residual Stresses and Strength Differential Effect in Discontinuously Reinforced Metal Matrix Composites, *Material Science and Engineering* Vol A183, pp 111-120, 1994

Kamat, S., J. Hirth and R. Mehrabian: Mechanical Properties of Particulate-Reinforced Aluminum-Matrix Composites, *Acta Metall.* Vol. 37, No. 9, pp. 2395-2402, 1989

Kujawski, D., Z. Xia and F. Ellyin: Morphology/Loading Direction Coupling on Transverse Behaviour of Composites, Proceedings of IUTAM Symposium on Microstructure Property Interactions in Composite Materials, Aalborg, Denmark, 1994, In press.

Lee, J. and K. Subramanian: Effect of Cold Rolling on the Elastic Properties of $(Al_2O_3)_p$-Al Composite, *Journal of Materials Science* Vol. 28, pp. 1578-1584, 1993

Levy, A. and J. Papazian: Elastoplasic Finite Element Analysis of Short-Fibre-Reinforced SiC/Al Composites: Effects of Thermal Treatment, *Acta Metall. Mater.* Vol. 39, No. 10, pp. 2255-2266, 1991

Levy, A. and J. Papazian: Tensile Properties of Short Fibre-Reinforced SiC/Al Composites: Part II. Finite-Element Analysis, *Metallurgical Transactions* Vol 21A, pp. 411-420, 1990

Llorca, J.: A Numerical Study of the Mechanisms of Cyclic Strain Hardening in Metal-Ceramic Composites, *Acta Metall. Mater.* Vol. 42, No. 1, pp. 151-162, 1994

Lloyd, D., Aspects of Fracture in Particulate Reinforced Metal Matrix Composites, *Acta Metall. Mater.* Vol. 39, No. 1, pp. 59-71, 1991

Llorca, J., A. Needleman and S. Suresh: An Analysis of the Effects of Matrix Void Growth of Deformation and Ductility in Metal-Ceramic Composites, *Acta Metall. Mater.* Vol. 39, No. 10, pp. 2317-2335, 1991

McDanels, D.: Analysis of Stress-Strain, Fracture and Ductile behaviour of Aluminum Matrix Composites Containing Discontinuous Silicon ide Reinforcement, *Metallurgical Transactions* Vol. 16A, pp. 1105-1115, 19.

Mochida, T., M. Taya and D. Lloyd: Fracture of Particles in a Particle/Metal Matrix Composite under Plastic Straining and Its Effect on the Young's Modulus of the Composite, *Materials Transactions, JIM* Vol. 32, No. 10, pp. 931-942, 1991

Mori, T. and K. Tanaka: Average Stress in Matrix and Average Elastic Energy of Materials with Misfitting Inclusions, *Acta Metall.* Vol. 21, pp. 571-574, 1973

Nardone, V. and K. Prewo: On the Strength of Discontinuous Silicon Carbide Reinforced Aluminum Composites, *Scripta Metallurgica* Vol. 20, pp. 43-48, 1986

Needleman, A.: A Continuum Model for Void Nucleation by Inclusion Debonding, *Journal of Applied Mechanics* Vol. 54, pp. 525-531, 1987

Shang, J. and R. Ritchie: On the Particle-Size Dependence of Fatigue-Crack Propagation Thresholds in SiC-Particulate-Reinforced Aluminum-Alloy Composites: Role of Crack Closure and Crack Trapping, *Acta Metall.* Vol. 37, No. 8, pp. 2267-2278, 1989

Shi, N., R. Arsenault, A. Krawitz and L. Smith: Deformation-Induced Residual Stress Changes in SiC Whisker-Reinforced 6061 Al Composites, *Metallurgical Transactions* Vol. 24 A, pp. 187-196, 1993

Taya, M. and K. Lulay: Strengthening of a Particulate Metal Matrix Composite by Quenching, *Acta Metall. Mater.* Vol. 39, No. 1, pp. 73-87, 1991

Tvergaard, V.: Analysis of Tensile Properties for a Whisker-Reinforced Metal-Matrix Composite, *Acta Metall. Mater.* Vol. 38, No. 2, pp. 185-194, 1990

Wang, Z., T. Chen and D. Lloyd: Stress Distribution in Particulate-Reinforced Metal-Matrix Composites Subjected to External Load, *Metallurgical Transactions* Vol. 24A, pp. 197-207, 1993

Withers, P., W. Stobbs and O. Pedersen: The Application of the Eshelby Method of Internal Stress Determination to Short Fibre Metal Matrix Composites, *Acta Metall.* Vol. 37, No. 11, pp. 3061-3084, 1989

Wu, J.: An Elasto-Plastic Material Model and Applications, Dissertation for Master of Science Degree, University of Alberta, 1989

Xia, Z. and F. Ellyin: Nonproportional Multiaxial Cyclic Loading: Experiments and Constitute Modelling, *Journal of Applied Mechanics Vol.* 58 or 113, pp. 317-325, 1991

Zahl, D. and R. McMeeking: The Influence of Residual Stress on the Yielding of Metal Matrix Composites, The Influence of Residual Stress on the Yielding of Metal Matrix Composites, *Acta Metall. Mater.* Vol. 39, No. 6, pp. 1117-1122, 1991

Appendix A: The Eshelby Tensor for a Spherical Inclusion

The Eshelby tensor used to determine the results shown in Chapter two is

$$
\begin{bmatrix}
\dfrac{7-5\nu}{15(1-\nu)} & \dfrac{-1+5\nu}{15(1-\nu)} & \dfrac{-1+5\nu}{15(1-\nu)} & 0 & 0 & 0 \\[2ex]
\dfrac{-1+5\nu}{15(1-\nu)} & \dfrac{7-5\nu}{15(1-\nu)} & \dfrac{-1+5\nu}{15(1-\nu)} & 0 & 0 & 0 \\[2ex]
\dfrac{-1+5\nu}{15(1-\nu)} & \dfrac{-1+5\nu}{15(1-\nu)} & \dfrac{7-5\nu}{15(1-\nu)} & 0 & 0 & 0 \\[2ex]
0 & 0 & 0 & \dfrac{2(4-5\nu)}{15(1-\nu)} & 0 & 0 \\[2ex]
0 & 0 & 0 & 0 & \dfrac{2(4-5\nu)}{15(1-\nu)} & 0 \\[2ex]
0 & 0 & 0 & 0 & 0 & \dfrac{2(4-5\nu)}{15(1-\nu)}
\end{bmatrix}
$$

Where ν is the Poisson's ratio.

For ellipsoid shape particles the Eshelby tensor is also dependent on the particle aspect ratio.

Appendix B: Flowchart of the FORTRAN Subroutine Implementing the Ellyin and Xia Constitutive Relation

```
                    ( Start )
                        │
        /Enter Material Properties /
        /  Data from last step    /
                        │
        │ Calculate proprotional limit │
                        │
        │ Form elastic stiffnes tensor │
                        │
  No  /  Was the previous stress  \
200 ◄─\  inside the yield surface? /
                    Yes │                          100
        │ Start In Yield Surface       │
        │ Calculate elastic stress increment │
        │ and q at the end of the increment │
                        │
  No  /  Is q less than the  \
150 ◄─\  proportional limit?  /
                    Yes │
                │ ERM = 1 │
                        │
        │ Calculate   stress—strain  tensor │
                        │                        150
        │ Calculate   ratio of elastic and │
        │             plastic parts        │
                        │
        │ Calculate elastic part of │
        │ the stress—strain tensor  │
                        │
        │ Calculate elastic stress/strain increment │
                        │
        │ Update the stress │
        │ at the yield point │
                        │
        │ Update the plastic strain length │
        │ at point of transition from      │
        │ elastic to plastic loading       │
                        │                        200
        /  Stress Point Is   /
        / On The Yield Surface /
                        │
        /  Elastic strain is zero /
```

```
100 ◄─  Elastic      Is is plastic loading
                     (or elastic unloading)?

                        Plastic │

                         Is the
              No        stress point         Yes
           ┌───────── inside the memory ──────────┐
           │               surface?               │
  │ Monotonic Plastic loading │        │ Plastic Reloading │
  │      ERM = 2              │        │     ERM = 3       │
           └──────────┬───────────────────┘
                      │
           │ Update Stress Strain │
           │ interpolation data   │
                      │
           │ Calculate the     │
           │ stiffness tensor  │
                      │
           │ Calculate elastic plastic │
           │ stress increment          │
                      │
       │ Calculate elastic and plastic │
       │ parts of the strain increment │
                      │
       │ Calculate the equivalent │
       │ plastic strain increment │
       │ and change in size of    │
       │ the yield surface        │
                      │
           │ Form the        │
           │ elastic plastic │
           │ stress strain   │
           │ tensor          │
                      │
       │ Calculate the movement  │
       │ of the yield and memory │
       │ surfaces                │
                      │
       │ Calculate stress at time │
       │ t + dt                   │
                      │
       / Update working array        /
       / for the next increment      /
```

96

Appendix C: Results From Cyclic Step Tests on 6061 Aluminum Alloy

Cyclic step tests where completed on specimens of 6061 aluminum alloy in T0

and T6 heat treatments. The strain amplitude was increased every 100 cycles until the

specimens failed.

The results for 6061-T0 are shown in figure C.1. When the loops are aligned, as

in figure C.2, it is clear that this is not a Masing material, i.e. the proportional limit

changes. A curve of the form $q_s = q_o + A\epsilon_{eqv,max} + B\epsilon_{eqv,max}^2$ was applied to the data for

$\Delta\epsilon/2$ and $q_s - q_m$ where q_m is the proportional limit under monotonic loading.

$\Delta\epsilon/2$	$q_s - q_m$ (MPa)
0.003	0.5
0.004	4.0
0.005	8.5

This results in A = -192.67 (MPa) and B = 378535 (MPa). The proportional limit is

assumed to remain constant, at a value of 42.5 MPa, after the maximum strain exceeds

0.005. This interpolation data used is:

Initial Curve		Stable Curve	
Stress (MPa)	Strain	Stress (MPa)	Strain
+3.500000E+01	+5.175973E-02	+4.000000E+01	+6.250000E-02
+4.102992E+01	+7.427133E-02	+4.855441E+01	+8.501160E-02
+5.097799E+01	+1.273344E-01	+6.459194E+01	+1.380747E-01
+6.051500E+01	+2.109489E-01	+7.473513E+01	+2.216892E-01
+6.757629E+01	+3.251148E-01	+8.033839E+01	+3.358551E-01
+7.296734E+01	+4.698323E-01	+8.439207E+01	+4.805726E-01
+7.762537E+01	+6.451011E-01	+8.905010E+01	+6.558414E-01
+8.190855E+01	+8.509215E-01	+9.333328E+01	+8.616617E-01
+8.566125E+01	+1.087293E+00	+9.708598E+01	+1.098034E+00
+8.894073E+01	+1.354216E+00	+1.003655E+02	+1.364957E+00
+9.197459E+01	+1.651691E+00	+1.033993E+02	+1.662431E+00
+9.453088E+01	+1.979717E+00	+1.059556E+02	+1.990458E+00

+9.671076E+01	+2.338295E+00	+1.081355E+02	+2.349035E+00
+9.994300E+01	+2.727424E+00	+1.113677E+02	+2.738164E+00
+1.021697E+02	+3.147105E+00	+1.135944E+02	+3.157845E+00
+1.045316E+02	+3.597337E+00	+1.159563E+02	+3.608077E+00

The results from the cyclic step test on the 6061-T6 aluminum alloy are shown in figures C.3 and C.4. In this case the proportional limit appears much greater at strain amplitudes at which very little plastic deformation occurs. When the strain amplitude is increased above the elastic strain limit the proportional limit quickly drops from 264 MPa to 154 MPa. This is reflected in the input data for 6061-T6.

Initial Curve		Stable Curve	
Stress (MPa)	Strain	Stress (MPa)	Strain
+1.540000E+02	+2.221451E-01	+1.555000E+02	+2.408242E-01
+1.648964E+02	+2.373534E-01	+1.647258E+02	+2.560315E-01
+1.901152E+02	+2.731994E-01	+1.864723E+02	+2.918775E-01
+2.291080E+02	+3.296839E-01	+2.181819E+02	+3.483620E-01
+2.788573E+02	+4.068070E-01	+2.555328E+02	+4.254851E-01
+3.069905E+02	+5.045686E-01	+2.847318E+02	+5.232467E-01
+3.176910E+02	+6.229689E-01	+3.039312E+02	+6.416469E-01
+3.237789E+02	+7.620077E-01	+3.143137E+02	+7.806857E-01
+3.274746E+02	+9.216850E-01	+3.180094E+02	+9.403631E-01
+3.299538E+02	+1.102001E+00	+3.204936E+02	+1.120679E+00
+3.317059E+02	+1.302956E+00	+3.222407E+02	+1.321634E+00
+3.327152E+02	+1.524549E+00	+3.232501E+02	+1.543227E+00
+3.342063E+02	+1.766780E+00	+3.247411E+02	+1.785458E+00
+3.359858E+02	+2.029650E+00	+3.265206E+02	+2.048328E+00
+3.372957E+02	+2.313159E+00	+3.278305E+02	+2.331837E+00
+3.379417E+02	+2.617306E+00	+3.284765E+02	+2.635984E+00

This data is provided graphically in figure 3.4. At strain higher than those achieved in the cyclic step tests the stable curve was assumed to run parallel to the initial curve.
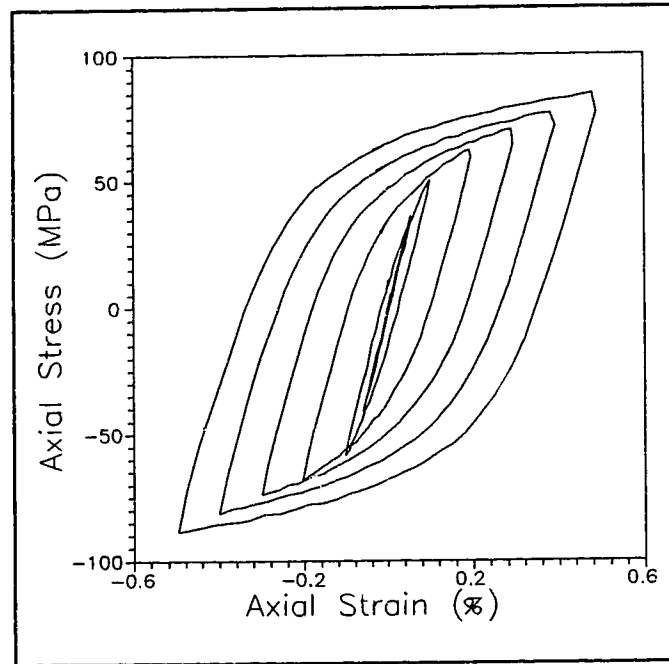
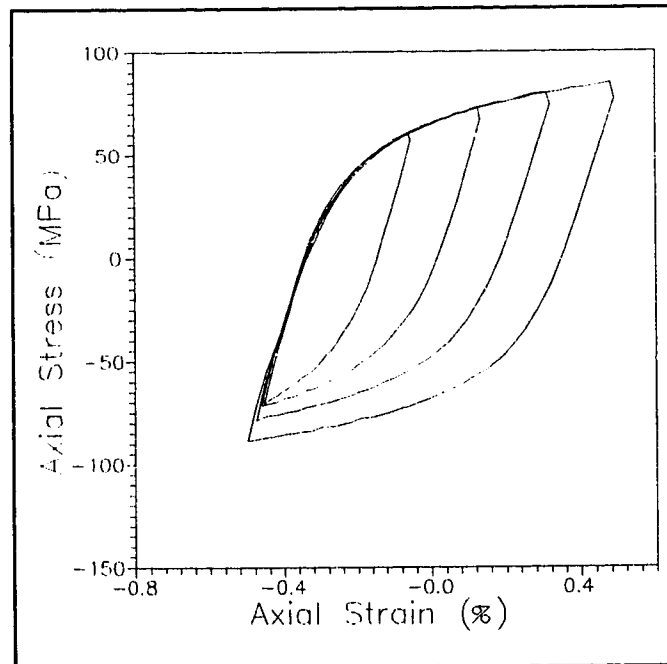Figure C.1: Results of the cyclic step test on 6061-TO aluminum alloy.

Figure C.2: The stable stress-strain curve is determined by aligning the stable loops.
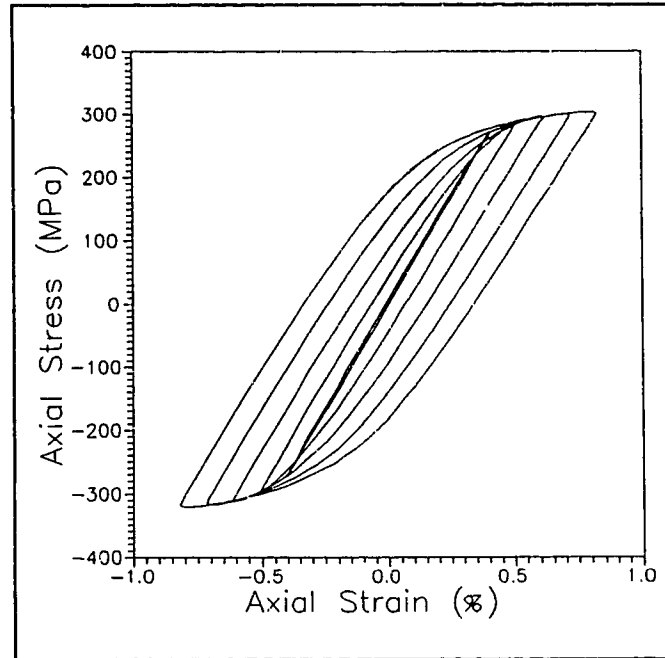
99

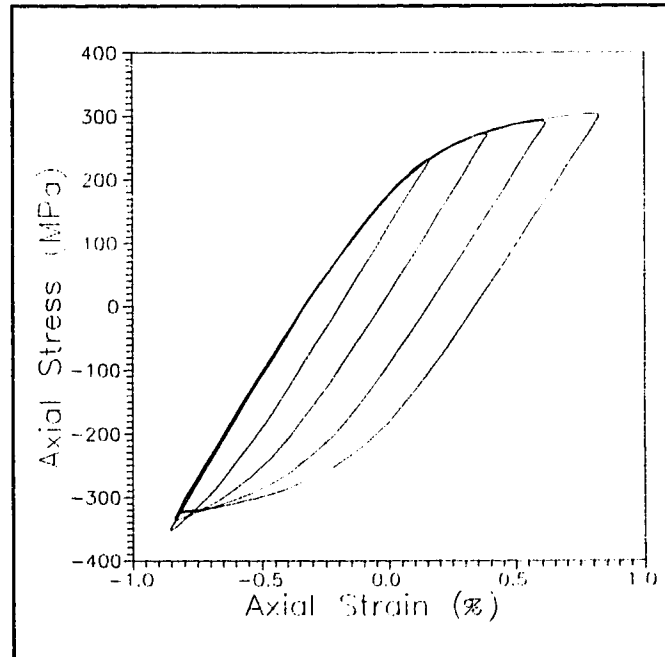Figure C.3: Results from the cyclic step test on 6061-T6 aluminum alloy.

Figure C.4: The aligned loops show that the proportional limit, for 6061-T6, quickly approaches 154 MPa.

100